AGU PUBLICATIONS

JGR

Journal of Geophysical Research: Atmospheres

RESEARCH ARTICLE

10.1002/2016JD025557

Low-CCN concentration air masses over the eastern North Atlantic: Seasonality, meteorology, and drivers

Robert Wood[1], **Jayson D. Stemmler**[1], **Jasmine Rémillard**[2], **and Anne Jefferson**[3]

[1]Department of Atmospheric Science, University of Washington, Seattle, Washington, USA, [2]School of Marine and Atmospheric Sciences, Stony Brook University, New York, New York, USA, [3]Cooperative Institute for Research in Environmental Sciences, Boulder, Colorado, USA

Key Points:
- A 20 month cloud condensation nuclei (CCN) data set from the Azores is used to identify air masses with very low concentrations
- Low-CCN air masses tend to occur during winter and spring and are often associated with cold air outbreaks occurring upstream of the Azores
- Liquid water path enhancement upstream of air mass arrival at the Azores can account for low concentrations via coalescence scavenging

Correspondence to:
R. Wood,
robwood2@uw.edu

Citation:
Wood, R., J. D. Stemmler, J. Rémillard, and A. Jefferson (2017), Low-CCN concentration air masses over the eastern North Atlantic: Seasonality, meteorology, and drivers, *J. Geophys. Res. Atmos.*, *122*, 1203–1223, doi:10.1002/2016JD025557.

Received 28 JUN 2016
Accepted 22 DEC 2016
Accepted article online 24 DEC 2016
Published online 30 JAN 2017

Abstract A 20 month cloud condensation nucleus concentration (N_{CCN}) data set from Graciosa Island (39°N, 28°W) in the remote North Atlantic is used to characterize air masses with low cloud condensation nuclei (CCN) concentrations. Low-CCN events are defined as 6 h periods with mean $N_{CCN} < 20$ cm^{-3} (0.1% supersaturation). A total of 47 low-CCN events are identified. Surface, satellite, and reanalysis data are used to explore the meteorological and cloud context for low-CCN air masses. Low-CCN events occur in all seasons, but their frequency was 3 times higher in December–May than during June–November. Composites show that many of the low-CCN events had a common meteorological basis that involves southerly low-level flow and rather low wind speeds at Graciosa. Anomalously low pressure is situated to the west of Graciosa during these events, but back trajectories and lagged SLP composites indicate that low-CCN air masses often originate as cold air outbreaks to the north and west of Graciosa. Low-CCN events were associated with low cloud droplet concentrations (N_d) at Graciosa, but liquid water path (LWP) during low-CCN events was not systematically different from that at other times. Satellite N_d and LWP estimates from MODIS collocated with Lagrangian back trajectories show systematically lower N_d and higher LWP several days prior to arrival at Graciosa, consistent with the hypothesis that observed low-CCN air masses are often formed by coalescence scavenging in thick warm clouds, often in cold air outbreaks.

1. Introduction

Cloud condensation nuclei (CCN) influence the radiative budget of the Earth through their activation to cloud droplets, the concentration of which (N_d) is a key determinant of cloud effective radius and therefore cloud optical thickness and albedo [*Boers and Mitchell*, 1994]. In many regions, the CCN concentration (N_{CCN}) has increased considerably over the industrial period [*Isaksen et al.*, 2009] and is thought to have led to an increase in cloud albedo, but the magnitude of the radiative forcing (RF_{aci}) from aerosols via these aerosol-cloud interactions is highly uncertain [*Intergovernmental Panel on Climate Change*, 2013]. Theoretical and modeling results show that the change in albedo associated with an increase in CCN is dependent not only upon the CCN perturbation but also upon N_{CCN} in the unperturbed state [*Carslaw et al.*, 2013]. This is both because the albedo of a cloud with a very low N_d is more susceptible to N_d increases than is the albedo of a cloud with a higher unperturbed N_d [*Platnick and Twomey*, 1994] and also because the relationship between N_{CCN} and N_d is concave [*Martin et al.*, 1994; *Ramanathan*, 2001; *Hudson et al.*, 2010]. These arguments support the notion that albedo responses are strongly sublinear to emissions [*Carslaw et al.*, 2013], although there are conflicting results regarding this degree of sublinearity [*Ghan et al.*, 2013]. Nevertheless, both *Carslaw et al.* [2013] and *Ghan et al.* [2013] demonstrate that a large fraction of the uncertainty in RF_{aci} can be attributed to uncertainty in the aerosol state of the preindustrial environment.

Recent studies have questioned the extent to which the present-day aerosol environment is pristine, i.e., unperturbed by anthropogenic impacts and therefore representative of preindustrial conditions. *Andreae* [2007] argues that unperturbed regions may be difficult to find in the Northern Hemisphere (NH), even over the oceans, and observational evidence at remote marine locations provides some support for this [*Hudson and Noble*, 2009; *Clarke et al.*, 2013] . *Hamilton et al.* [2014] quantified the degree of pristineness by using preindustrial and present-day emissions in two simulations of a global model, forced with identical meteorology, to identify the fraction of days on which low-altitude N_{CCN} in the preindustrial and present day differ by more than 20%. Over the NH oceans, their results indicate very few days that are pristine by this metric. Curiously, the few pristine days that do occur over the NH oceans in their model occur in summertime, when observations

suggest higher N_{CCN} than during winter [*Wood et al.*, 2015]. There is not necessarily a conflict here, however, because low concentrations are not, by themselves, necessarily indicative of pristineness. That said, it is reasonable to imagine that in many instances, low N_{CCN} is likely to be indicative of a lack of pollution aerosol. Further, as it is not possible to observe the preindustrial aerosol environment directly, it seems important to devote attention to low-CCN environments and the processes controlling them.

Observations from many marine boundary layers (MBLs) show that there is a large degree of spatiotemporal variability in N_{CCN} and N_d in the MBL [e.g., *Martin et al.*, 1994; *Heintzenberg et al.*, 2000; *Miles et al.*, 2000; *Allen et al.*, 2011]. The causes of this variability remain poorly understood, particularly the extent to which sources or sinks control the variability. During certain meteorological conditions it is clear that precipitation-driven removal of cloud droplets (and hence CCN) can dramatically reduce CCN concentrations over mesoscale regions [*Wang et al.*, 2010; *Terai et al.*, 2014; *Berner et al.*, 2013; *Goren and Rosenfeld*, 2015], which can introduce considerable temporal and spatial variability. Theoretical and modeling studies [e.g., *Feingold et al.*, 1996; *Mechem et al.*, 2006; *Wood*, 2006] demonstrate that coalescence scavenging, i.e., the removal of cloud droplets by collision-coalescence, is a key mechanism for CCN removal from the MBL. Observational evidence also supports this [*Hudson et al.*, 2015]. Some studies argue that this mechanism may be important for explaining land-ocean CCN contrasts [*Baker and Charlson*, 1990] and geographical variability of time-mean N_{CCN} over oceans [*Wood et al.*, 2012]. Further, it is clear that the rate of loss of N_{CCN} by coalescence scavenging increases strongly with the availability of liquid water [*Feingold et al.*, 1996; *Wood*, 2006]. Coupling these findings with the observed dependence of precipitation rate on cloud liquid water path (LWP) and cloud thickness [e.g., *Comstock et al.*, 2004; *VanZanten et al.*, 2005], it has been shown that MBL-averaged loss rates from coalescence scavenging are approximately proportional to the square of the LWP (or the fourth power of cloud thickness), such that CCN rates are negligible for LWP < 50 g m^{-3} but become comparable to surface and entrainment CCN sources for LWP ~ 100 g m^{-3} and are dominant CCN sinks ($\sim$100 cm^{-3} day^{-1}) for LWP > 200 g m^{-3} [*Wood*, 2006].

There has been little systematic study of low-N_{CCN} conditions to explore the factors controlling CCN variability in the clean MBL. We know that catastrophic reductions in CCN can occur and that these can help drive cloudiness transitions in the tropical and subtropical MBL, e.g., closed to open mesoscale cells [*Berner et al.*, 2013]. There is evidence of similar behaviors in midlatitudes [*Wood et al.*, 2015], and very low N_d concentrations (<20 cm^{-3}) have been observed in subtropical and midlatitude stratocumulus [*Hindman et al.*, 1994; *Boers et al.*, 1998], in cold air outbreaks [*Field et al.*, 2014] and in the high Arctic [*Mauritsen et al.*, 2011]. *Twomey and Wojciechowski* [1969] examined a large amount of aircraft-derived CCN data over the remote oceans and found a typical timescale of 3 days for the relaxation of the CCN population to the low values typical of remote marine air, and *Goren and Rosenfeld* [2015] provide a recent detailed satellite case study of the transition from a continental to a marine air mass over the eastern Atlantic showing how the cloud droplet concentration N_d decreases in low clouds advecting from the continent due to coalescence scavenging.

In this study, we take advantage of a long, continuous record (20 months) of CCN and other aerosol and cloud data sets at a remote North Atlantic island site that straddles the boundary between the subtropics and the midlatitudes. We focus on exploration of the meteorological and cloud conditions associated with low N_{CCN} events at the site. Section 2 describes the data sets to be used and the methodology for case selection. Section 3 presents a composite analysis of meteorological conditions for the low-N_{CCN} cases, and section 4 provides an analysis of the multiday Lagrangian history of low N_{CCN} air masses reaching the site. Section 5 discusses potential mechanisms for low-CCN events, section 6 introduces a conceptual model, and section 7 provides conclusions and suggestions for further study.

2. Data and Methodology

At the core of this analysis are data from the 20 month Clouds, Aerosol, and Precipitation in the Marine Boundary Layer (CAP-MBL) field deployment of the ARM Mobile Facility (AMF) on Graciosa Island in the Azores [*Wood et al.*, 2015]. The facility operated from April 2009 until December 2010 and provided a number of important in situ and surface-based remote sensing observations. Details of the specific data sets used can be found in section 2.1. In addition to the AMF site products, we use meteorological reanalyses from the ERA-interim product (described in section 2.2), 8 day back trajectories to provide information on air mass histories (section 2.3), and satellite data from the MODIS instrument aboard the NASA Aqua and Terra satellites to provide larger spatial context of the cloud properties (section 2.4).

Table 1. AMF Instruments and Data Products Used in This Study

Measurement	Symbol	Instrument/References
Cloud condensation nucleus number concentration at 7 supersaturations S from 0.1 to 1.2%	N_{CCN}	CCN counter (DMT Model 1) *Roberts and Nenes* [2005]
CN concentration N_{CN} (all particles larger than 10 nm)	N_{CN}	TSI 3010 counter
Aerosol dry scattering coefficient (450, 550, 700 nm)	σ	TSI 3563 nephelometer
Near-surface wind speed and direction (10 m altitude)	u_{10}	Propeller/vane (RM Young 05103)
Liquid water path	LWP	23.8 and 31.4 GHz microwave radiometers (MWR) *Turner et al.* [2007]
Cloud droplet concentration	N_d	Narrow field of view radiometer and MWR *McComiskey et al.* [2009]
Cloud boundaries and types from *Rémillard et al.* [2012]		Zenith W-band (95 GHz) ARM cloud radar Vaisala ceilometer (CL31)

2.1. AMF Data

The CAP-MBL field deployment of the AMF provided a wealth of data from Graciosa island (39.1°N, 28.0°W), a small island in the Azores archipelago situated in the remote eastern North Atlantic approximately 1600 km west of Lisbon, Portugal, and roughly 4200 km east of Washington, DC. Table 1 details the measurements and instruments used in this analysis.

2.1.1. CCN, CN, and Aerosol Scattering

Several in situ aerosol measurements from the AMF Aerosol Observing System (AOS) are used in this study. The key variable used to define events in this study is the CCN concentration. CCN measurements are made using a commercially available Droplet Measurement Technologies (DMT) Model 1 CCN counter [*Roberts and Nenes*, 2005], which measures the N_d at seven supersaturations S (nominally 0.1, 0.2, 0.4, 0.6, 0.9, 1.1, and 1.2%). The counter is programmed to step through the different S and varies them by varying the temperature of the chamber walls, with a complete cycle of all seven S made every 30 min. S is calculated using a heat transfer and fluid dynamics flow model [*Lance et al.*, 2006]. To ensure the highest quality CCN measurements, we only include data for those times when the instrument temperature, and hence S, is stable. Stable measurements in each S step are averaged together to generate one CCN "measurement" at each S approximately every 30 min. The CCN instrument was serviced and calibrated at the beginning the AMF deployment. During the early part of the CAP-MBL campaign the CCN counter appeared to function correctly, but during late 2009 and early 2010 it was clear that the CCN counts were decreasing at a rate that seemed suspiciously large. A time series of monthly mean N_{CCN} (Figure 1) indicates that N_{CCN} began to decrease after September 2009 and continued to decrease until the problem was noticed in June 2010, after which the CCN instrument was thoroughly serviced and calibrated and the concentrations returned to values typical of the same time during the previous year. Because the decline was gradual, the problem was not identified for several months. Despite this, an approach was developed to correct the CCN data using the CN counter as a reference. This correction is described in Appendix A, and only corrected CCN data are used in this study.

In addition to N_{CCN}, we use CN concentration N_{CN} measurements from a TSI 3010 model collocated with the CCN counter that provides the concentration of all particles greater than approximately 10 nm in diameter. We also use in situ aerosol scattering measurements from the AOS nephelometer system, which is collocated with the CCN counter and measures total dry aerosol scattering at three wavelengths. In this study, we use the submicron and sub-10 μm (total) aerosol scattering coefficient at 450, 550, and 700 nm wavelength.

2.1.2. Surface Wind and Cloud Measurements

Surface wind direction and speed measurements are made at an altitude of 10 m above ground at the Graciosa site using an RM Young propeller and vane anemometer system (Table 1). We use these data to contrast the wind speed and direction for low N_{CCN} events with those for non-low N_{CCN} conditions.

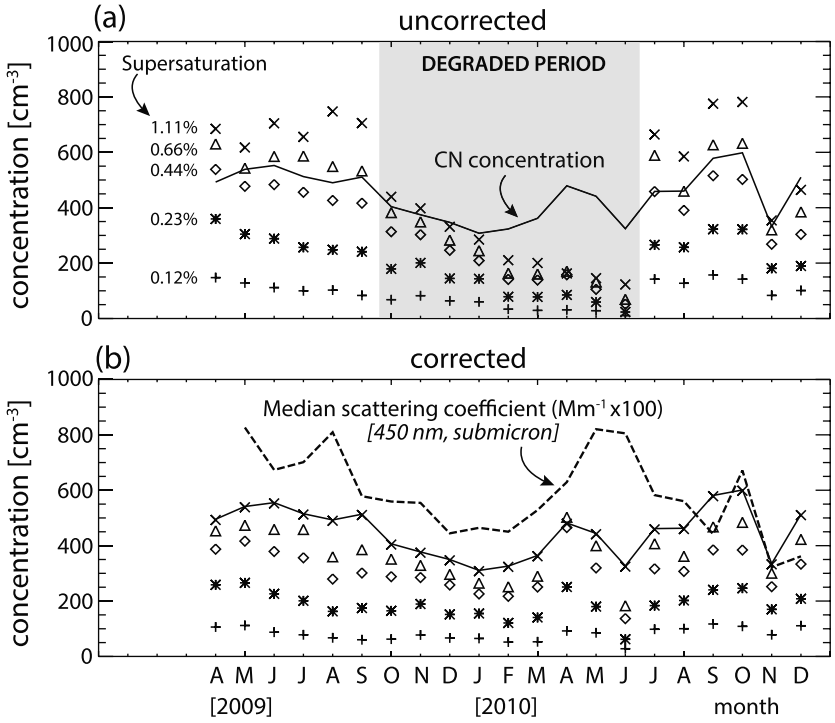

Figure 1. (a) Time series of monthly mean particle concentrations from the CCN counter (symbols), for five different supersaturations, with different symbols indicating different supersaturations listed in Figure 1a immediately to the left of the symbols. Monthly mean N_{CN} is shown as the solid line. Prior to construction of monthly mean values, to avoid contamination by local pollution, individual measurements (typically 4 min for a CCN measurement at a single supersaturation) that have high concentration variance are screened out by removing cases where the relative standard deviation (standard deviation/mean) exceeds unity. The period where the CCN counter was degraded is shown in gray. (b) CCN concentrations after the correction procedure has been applied. N_{CN} is also shown as in Figure 1a. Also shown in Figure 1b is a time series of the monthly median submicron blue (450 nm) aerosol scattering coefficient.

In this study, we use surface remotely sensed LWP retrievals based on the algorithm developed by *Turner et al.* [2007] that uses the 23.8 and 31.4 GHz channels from the passive microwave radiometer (MWR) situated at the Graciosa site. The LWP retrievals used are from the entire deployment, and have a time interval that is typically 20–30 s. In this study, we use the LWP retrievals to produce a comparison of the PDFs for low N_{CCN} events with those at other times.

Cloud boundaries and types are taken from the hour cloud product described in *Rémillard et al.* [2012]. Cloud types are based on data from the zenith pointing ARM W-band (95 GHz) cloud radar and a Vaisala lidar ceilometer (model CT25K prior to mid-July 2010, and a model CL31 after that). In this study we use the occurrence of four basic cloud types: high clouds with bases above 7 km; midlevel cloud layers with bases at altitudes of 3–7 km; low-level clouds with bases and tops below 3 km; deep boundary layer clouds, with bases below 3 km but cloud tops above 3 km [see *Rémillard et al.*, 2012, Table 2].

2.2. Meteorological Analyses

Horizontal wind, pressure, and temperature fields from the ERA-Interim reanalysis [*Dee et al.*, 2011] are used to assess aspects of the large-scale meteorological fields associated with low-CCN events. In this study we use reanalysis fields every 6 h (at 00, 06, 12, and 18 UTC). Note that at the Azores, local and UTC time are within an hour of each other (local time = UTC −1 h). Reanalyses are used to illustrate individual events and to create composite fields for all low-CCN events, allowing us to contrast the composite meteorology with the seasonally varying mean meteorology. Anomalies for an instantaneous meteorological field are determined by subtracting a 30-day centered running mean field. These allow us to better isolate the synoptic meteorological differences associated with low-CCN events; without taking anomalies, because low-CCN events tend to occur during certain seasons, composites of absolute rather than anomaly fields may reflect the seasonal cycle rather than the key synoptic meteorology.

Using the ERA-Interim reanalyses, we also calculate the marine cold air outbreak (MCAO) index μ defined in *Kolstad and Bracegirdle* [2007] and *Kolstad et al.* [2009] as

$$\mu = \frac{\theta_{SST} - \theta_{700}}{p_0 - p_{700}} \quad (1)$$

where θ_{SST} is the potential temperature derived from the sea surface temperature (SST), θ_{700} is the potential temperature at 700 hPa altitude, p_0 is the sea level pressure, and $p_{700} = 700$ hPa. The MCAO index defined in (1) is calculated every 6 h at the times that ERA-Interim data are available. Larger values of μ indicate weaker lower tropospheric stability, consistent with cold lower tropospheric air overlying a warmer surface. Positive values of μ are often taken as being indicative of cold air outbreak conditions [*Kolstad et al.*, 2009].

2.3. Trajectories

Three-dimensional 8 day back trajectories were computed 4 times daily for the entire AMF deployment using the full 3-D NOAA Hybrid Single-Particle Lagrangian Integrated Trajectory (HYSPLIT) trajectory model [*Draxier and Hess*, 1998]. Back trajectories end at 500 m above sea level at Graciosa at 03, 09, 15, and 21 UTC, i.e., at the midpoint of each 6 h period used to aggregate the CCN data (see section 3 below) and are constructed for every 6 h period during the deployment. The trajectories are driven by the National Centers for Environmental Prediction Global Data Assimilation reanalysis product at 1 × 1° resolution [*Kalnay et al.*, 1996]. Back trajectories provide a more comprehensive understanding of the air masses along their path to the Azores. Meteorological analysis data, especially the MCAO index (section 2.2), are also interpolated onto the trajectories as a function of time to provide a time history of the Lagrangian evolution of meteorology along trajectories.

2.4. Satellite Data Sets

Satellite data are taken from the Moderate Resolution Imaging Spectroradiometer (MODIS) on both the NASA Aqua and Terra satellites, which pass over Graciosa at approximately 10:30 A.M. and 1:30 P.M. local time. Only daytime data are used. We use daily level 3 products [*Oreopoulos*, 2005] for each satellite, which aggregate MODIS collection 5 retrievals of LWP and effective radius for liquid-topped cloud [*King et al.*, 1997] to a 1×1° spatial grid. These products are then used to compute droplet number concentration N_d at 1×1° applying the method of *Boers et al.* [2006] and *Bennartz* [2007], with assumptions detailed in appendix A of *Grosvenor and Wood* [2014]. To mitigate known problems with retrievals in broken or ice cloud conditions, N_d data are accepted only for those 1×1° boxes where the total cloud fraction is equal to the single layer liquid cloud fraction and exceeds 60%.

We then spatiotemporally colocate the MODIS level 3 data with the back trajectory locations (section 2.3) to produce a sparse time series of MODIS-retrieved properties along the path of each trajectory. To constitute a match in time and space between the satellite data and trajectories, we search for available MODIS data within a 3 × 3° box around the trajectory location at the times of the MODIS overpasses. Any level 3 box within this range is considered to be associated with the trajectory. The resulting MODIS time series are composited as a function of time prior to the air mass arrival at Graciosa, and this compositing is carried out separately for trajectories that end at Graciosa during low N_{CCN} and non-low N_{CCN} events, which allows us to contrast the liquid cloud property histories for these subsets.

3. Composite Analysis of Low-CCN Events

In this section we define the low-CCN events and then composite these events to identify meteorological properties associated with the events. We compare the composite meteorology with all the data to understand differences between low-CCN events and non-low-CCN cases. To define low-CCN events, we first average N_{CCN} for *Ss* from 0.0 to 0.15% over 6 h periods (0–6, 6–12, 12–18, and 18–24 UTC). Most of the measurements in this 0.0–0.15% *S* range are made at an *S* close to 0.1% (95% of the individual *S* values range from 0.11 to 0.125%). This 6 h mean time series we term $\overline{N_{CCN,0.1\%}}$. Any given 6 h period is defined to be a low-CCN event if $\overline{N_{CCN,0.1\%}}$ <20 cm^{-3}. We use 6 h periods as this is sufficiently long to provide a characterization of N_{CCN} in an air mass, while being short enough to capture variations in air mass properties. Using this definition, we identify a total of 47 low-CCN events. These events constitute approximately 2% of the total number of 6 h periods (of which there are 2262 with CCN data and 223 periods with missing data). Of the 47 low-CCN periods identified, 22 are isolated 6 h periods, 8 consist of two consecutive 6 h periods, and 3 consist of three consecutive 6 h periods. The distribution of N_{CCN} measurements (taken approximately every

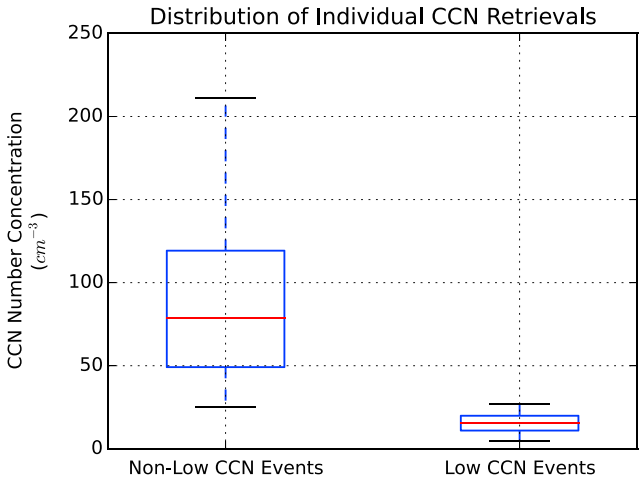

Figure 2. Box-whisker plots showing the distribution of all CCN measurements (not simply 6 h means) at $S = 0.1\%$ for the (left) non-low and (right) low-CCN events during the entire deployment. Boxes show 25th, 50th (red line), and 75th percentiles, and whiskers reach out to show the 5th and 95th percentiles.

30 min as described in section 2.1.1) at 0.1% S during low-CCN events is contrasted with the distributions for non-low-CCN events (Figure 2). The median $\overline{N_{CCN,0.1\%}}$ is approximately a factor of 4 higher during non-low-CCN events than during low-CCN events. We choose to focus on a relatively small set of 33 extreme events here to provide a manageable set of cases that can be explored both individually and statistically.

Low-CCN events were much more common during winter (December-January-February, DJF) and spring (March-April-May, MAM) than during summer (June-July-August, JJA) and autumn (September-October-November, SON) as shown in Figure 3. Almost three quarters of the low-CCN events during the deployment occurred during winter and spring, despite the lower availability of data from these seasons due to the deployment not sampling a complete 2 year period. Factoring out the greater data availability in some seasons, it is 3 to 4 times more likely for a low-CCN event to occur during winter and spring than it is during summer and autumn (Figure 3). This preference for winter and spring did not simply track the seasonal mean (or median) N_{CCN}, which did not vary particularly strongly across seasons. Median CCN concentrations $N_{CCN,0.1\%}$ for all data are 60, 78, 80, and 79 cm^{-3} for DJF, MAM, JJA, and SON, respectively. So although median wintertime $N_{CCN,0.1\%}$ was lower than it was during other seasons, springtime median $N_{CCN,0.1\%}$ was as high as the medians for summer and autumn. This finding is reconciled because the spread of N_{CCN} during spring is larger than that during summer and fall, allowing there to be more low-CCN events without a major change in the median concentration.

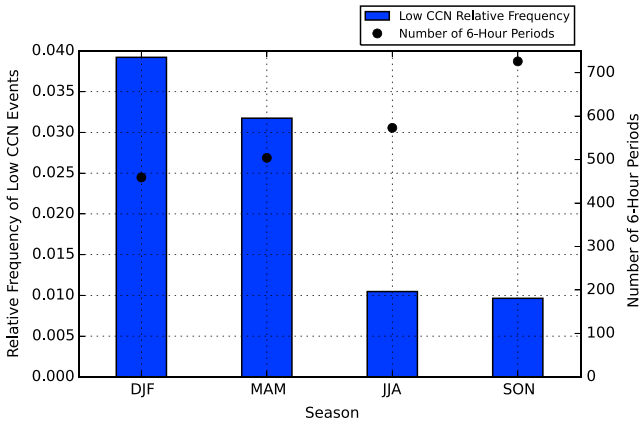

Figure 3. Winter and spring are the dominant seasons for low-CCN events at Graciosa. The figure shows the frequency of occurrence of low-CCN events (number of 6 h events/number of available 6 h periods) by season (blue bars, left axis) and the total number of 6 h time periods of available data for each season (black circles, right axis).

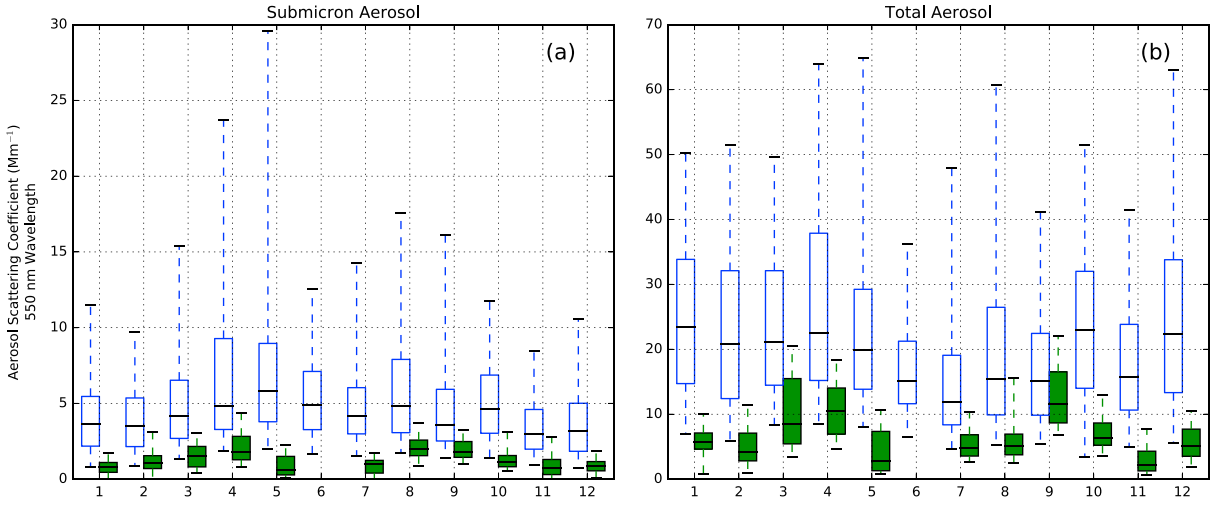

Figure 4. Aerosol scattering is reduced during low-CCN cases both for submicron and sub-10 μm particles. Monthly mean climatology (Jan = 1, Dec = 12) of (a) submicron and (b) total (sub-10 μm) aerosol scattering coefficient at 550 nm wavelength for low-CCN cases (green box-whiskers) and for non-low-CCN cases (blue). Boxes show 25th, 50th (line), and 75th percentiles, and whiskers reach out to show the 5th and 95th percentiles.

After dividing the 6 h periods into two categories (low-CCN events and non-low-CCN periods) we examine a variety of in situ and large-scale meteorological variables and examine any clear differences that exist between the subsets.

3.1. Aerosol Scattering

As with the CCN data, mean submicron dry scattering coefficient at 550 nm is determined for the same 6 h periods, and these are composited for low-CCN and non-low-CCN events. Figure 4 shows monthly mean aerosol scattering coefficients for the low and non-low-CCN cases, clearly demonstrating a major and systematic reduction in both fine and coarse mode aerosol scattering during low-CCN events in all months. The relative reduction of aerosol scattering during low-CCN events (compared with non-low-CCN events) appears to be roughly proportional to the reduction in N_{CCN} itself and is not strongly wavelength dependent (Figure 5). Median scattering is approximately a factor of 3 to 4 lower during low-CCN events than for non-low events, which is close to the factor of 4 difference in $N_{CCN,0.1\%}$ (Figure 2). The similar relative suppressions of scattering and $N_{CCN,0.1\%}$ during low-CCN events is consistent with the general relationship between dry scattering and N_{CCN} observed at a number of different continental and marine sites [*Jefferson*, 2010; *Shinozuka et al.*, 2015].

Aerosol scattering is often used as a proxy for N_{CCN} [e.g., *Shinozuka et al.*, 2015]. We conducted tests to explore the use of the submicron dry scattering coefficient at 450 nm wavelength ($\sigma_{450,sub}$) as an alternative approach to define "low-scattering" events in place of the CCN observations. Scattering and N_{CCN} are well correlated. The correlation coefficient r between 6 h mean $\sigma_{450,sub}$ and N_{CCN} is $r = 0.76$ ($S = 0.1\%$) and $r = 0.71$ ($S = 0.4\%$). Defining low-scattering events as those with 6 h mean $\sigma_{450,sub} < 1.5$ $(Mm)^{-1}$, we identify a similar number of events (53 total). Of these events, 20 of them are identical periods to those identified as low-CCN events, and a further 13 are periods that adjoin low-CCN periods. As with low-CCN events, low-scattering events occur most frequently in winter. The largest difference in the seasonality occurred in spring, during which time there were few low-scattering events but a considerable number of low-CCN events (not shown). We note that spring 2010 is when the correction made to CCN concentrations was the largest (see Appendix A), and so differences may reflect lingering issues with the CCN data or may reflect physical differences between scattering and N_{CCN}. Comparisons of meteorological data show that low-scattering events had similar wind roses and meteorological composite fields to those derived from low-CCN events (not shown). The findings are also not strongly sensitive to the choice of S used for the CCN measurement. Thus, the key conclusions of this study are largely robust to the specific choice of aerosol data used to define events.

3.2. Meteorology

In this section we examine two meteorological components; surface winds and sea level pressure. These provide some preliminary insight into the history and path of the air masses prior to reaching the Azores. Surface winds and mean sea level pressure are analyzed using both in situ observations as well as model reanalysis data to provide a large-scale picture of these variables.

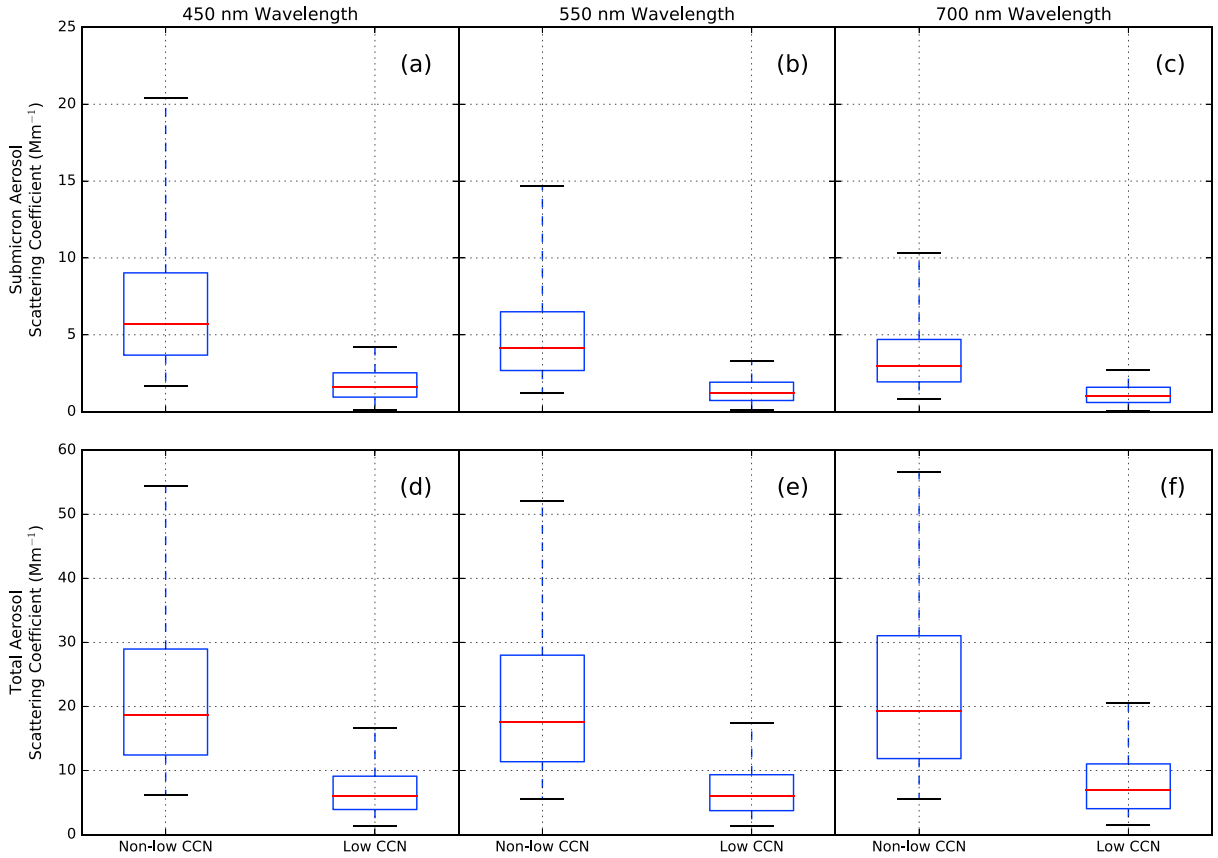

Figure 5. Aerosol scattering is reduced for low-CCN at all wavelengths and for both submicron and sub-10 μm particles. Figure shows box-whisker histograms (see caption for Figure 2) for low-CCN events (right bars in each panel) and for non-low-CCN events (left bars). (a–c) For submicron scattering and (d–f) for sub-10 μm scattering. Each column of panels shows a different wavelength: 450 nm (Figures 5a and 5d), 550 nm (Figures 5b and 5e), and 700 nm (Figures 5c and 5f).

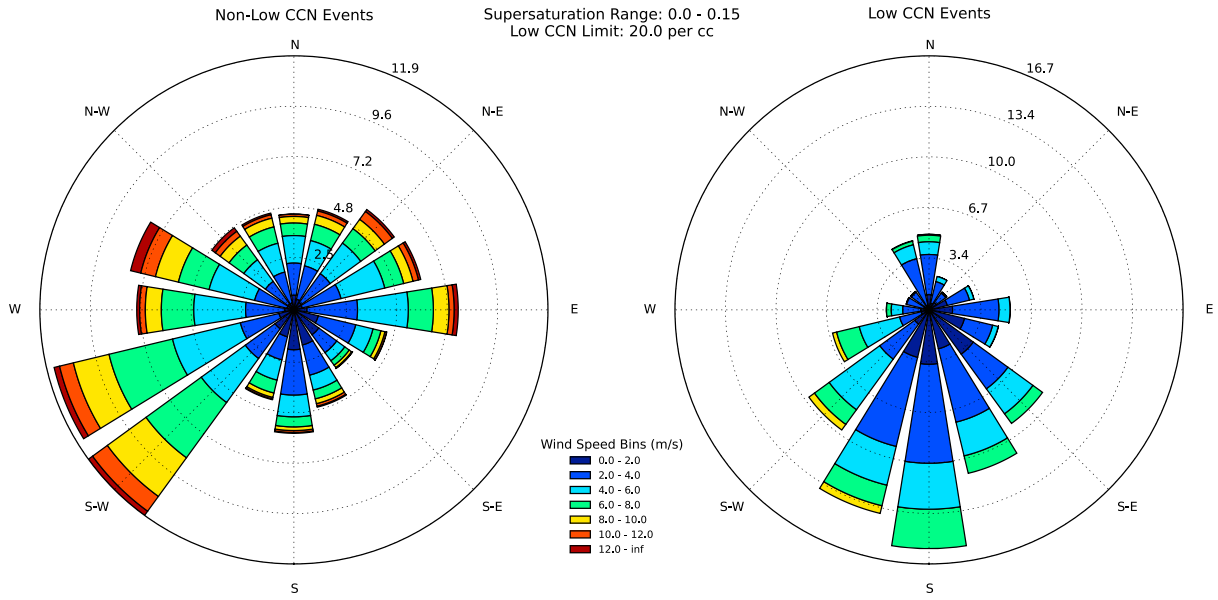

Figure 6. Low-CCN cases tend to occur during conditions of weak southerly surface winds. Surface wind rose PDFs for (left) non-low-CCN and (right) low-CCN events. The length of the radial bars is the relative frequency of winds of a given direction, and the colors indicate the frequency of different wind speeds. The distribution of wind speed and direction is markedly different for the low-CCN events.

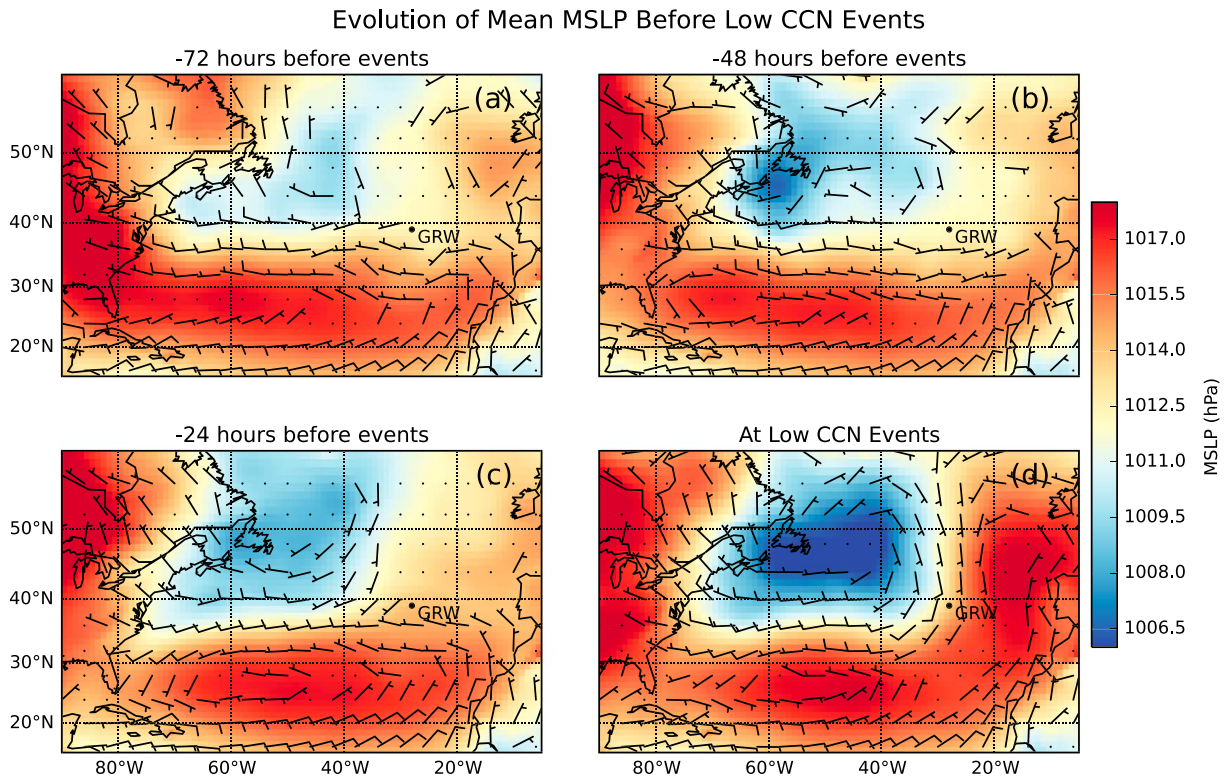

Figure 7. Composite mean sea level pressure (MSLP) for low-CCN events (a) 72 h, (b) 48 h, (c) 24 h prior to, and (d) at the start of low-CCN events at Graciosa. The location of Graciosa is marked as GRW. Mean barbs are also shown with mean wind speeds in knots (full barb = 10 kt; half barb = 5 kt).

One of the clearest examples of meteorological differences between low-CCN events and non-low-CCN cases at Graciosa is in the surface (10 m) winds (Figure 6). Surface winds during low-CCN events are considerably weaker and more southerly than at most other times. The median wind speed during low-CCN events was 3 m s^{-1} compared with almost 5 m s^{-1} for non-low events. The low wind speeds during low-CCN events would be associated with weaker sea spray particle fluxes [*Lewis and Schwartz*, 2004], and this may help explain why the total aerosol scattering, with a significant contribution from the coarse mode, was also lower during these periods. However, the clear distinction in wind *direction* suggests that air mass history may also be relevant. We return to the possible mechanisms causing low-CCN events in section 5.

To further assess the large-scale meteorological conditions associated with low-CCN events, we composite ERA-Interim reanalysis surface winds and mean sea level pressure (MSLP) fields for low-CCN events (Figure 7). At the start of low-CCN events (Figure 7d), Graciosa was typically situated under conditions of large-scale southerly flow, a picture consistent with the wind roses (Figure 6). However, the SLP anomalies at the times of the events alone present a misleading idea of the air mass origins. For several days prior to the low-CCN events, the average flow tends to be quite zonal (Figures 7a–7c), with a broad area of low pressure from 40 to 55°N and from 30 to 70°W. During the winter months, air flowing off the North American continent will be cold and will therefore likely experience strong surface temperature increases as it flows over the relatively warmer water of the North Atlantic.

However, because low-CCN events tend to occur more frequently during certain seasons (Figure 3), the absolute MSLP composite maps potentially alias in the large-scale seasonal variability and may not reflect synoptic events. Thus, we also examine composite differences (low-CCN events/non-low-CCN cases) with the seasonal cycle removed (see section 2.2). Figure 8 shows that at the start of the low-CCN events, on average there was an anomalous surface low center to the northwest of Graciosa and a high-pressure center to the east and north. The anomalously low surface pressure also extended down the entire North American eastern seaboard. The SLP anomalies prior to the low-CCN events (Figures 8a–8c) were generally smaller in magnitude and spatial scale and did not persist from day to day, other than anomalously low pressure consistently along the eastern

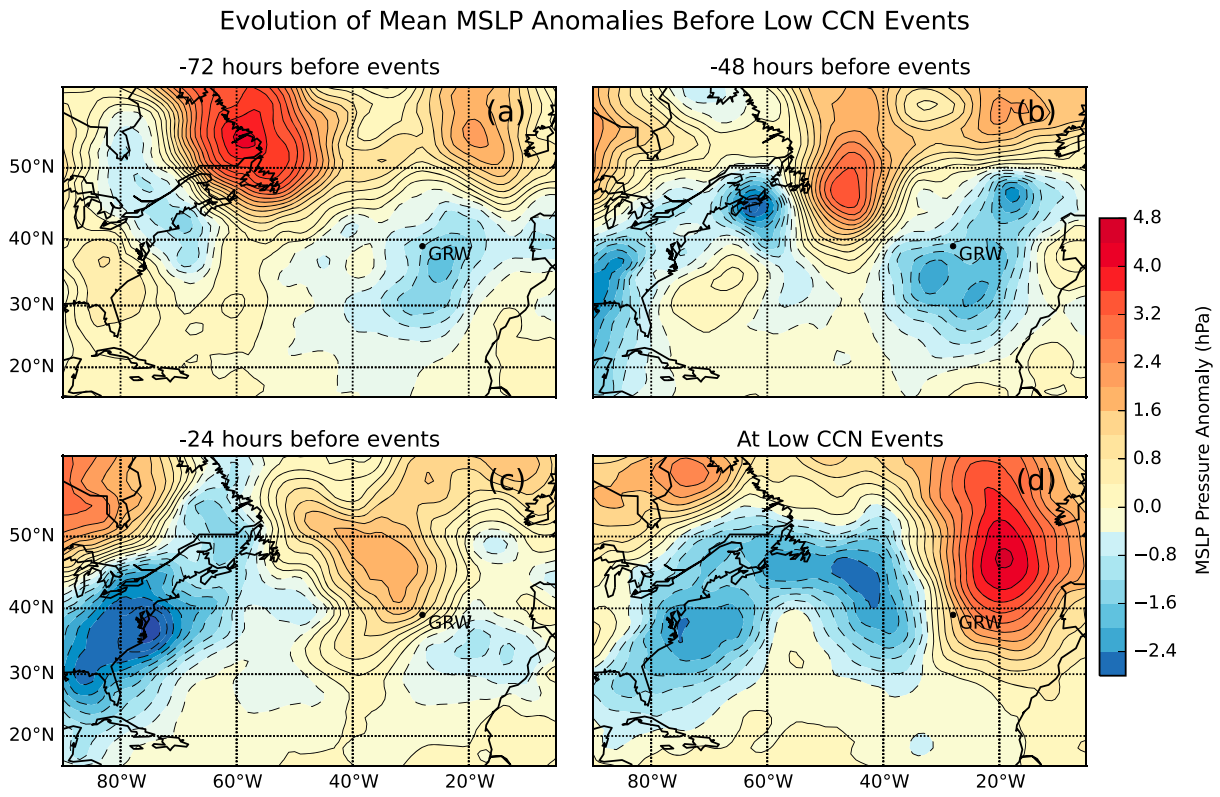

Figure 8. Composite difference in SLP anomalies (30 day running mean SLP removed) between low-CCN events and non-low-CCN cases. The panels show the anomalies (a) 72 h, (b) 48 h, and (c) 24 h prior to the low-CCN events at Graciosa and (d) during the low-CCN events. SLP fields for the low-CCN cases are taken from the beginning of the 6 h period of the event. The location of Graciosa is marked as GRW.

seaboard of North America. This indicates that the absolute MSLP composite maps (Figure 7) provide a reasonable assessment of the mean synoptic flow during low-CCN events.

3.3. Cloud Properties

We examine some of the major cloud properties associated with low-CCN events at the Graciosa site. There is little to distinguish distributions of LWP during low-CCN events from distributions at other times (Figure 9), suggesting that cloud differences local to the island and during the events themselves may not play a significant role in driving low-CCN events. Distributions of LWP for different seasons show some differences between low and non-low-CCN events, but there is no systematic difference across seasons, indicating no clear association between local LWP at Graciosa and the occurrence of low-CCN events (Figure 9).

Cloud fraction histograms observed from the ground at Graciosa for low-CCN events are contrasted with those for non-low-CCN cases in Figure 10. Hourly cloud fraction histograms are shown for the four cloud types (see section 2.1.2) and for the overall cloud cover (Figures 10e and 10j). Statistically, both low and non-low-CCN events show similar distributions of cloud cover for various cloud types, but there are some differences. There is a somewhat lower fraction of exclusively boundary layer clouds at Graciosa during low-CCN events, but there is a higher fraction of deep boundary layer clouds, midlevel clouds, and cirrus, all of which are associated with frontal systems in this region. This seems consistent with there generally being a low pressure situated to the north and west of Graciosa during low-CCN events.

Although the contrasts between cloud macrophysical variables at Graciosa during low-CCN events and other times is muted, N_d from the NDROP data product [*Riihimaki et al.*, 2014; *McComiskey et al.*, 2009] measured from surface remote sensing over Graciosa (Figure 11) are markedly lower during low-CCN events than at other times. During low-CCN events, there is only a 5% chance that the 6 h median N_d will exceed 100 cm^{-3}, whereas a high N_d tail extends to almost 400 cm^{-3} at other times. The median N_d during low-CCN events is approximately 3 times lower than at other times, consistent with the ratio of N_{CCN} (Figure 2). This is consistent with there being a sizeable Twomey effect associated with the contrast between periods of low and non-low CCN.

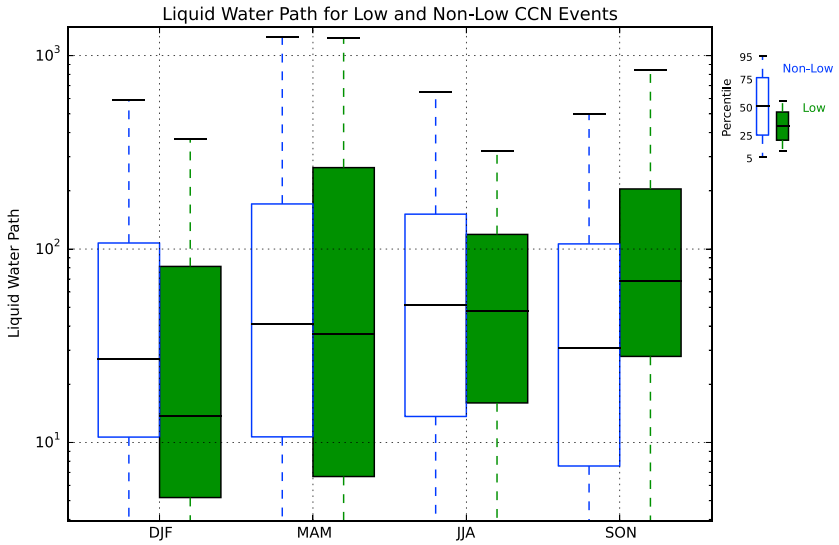

Figure 9. LWP distributions (units g m^{-2}) from the ground-based MWR at Graciosa for low-CCN cases (solid green box-whiskers) and for non-low-CCN cases (open blue box-whiskers), broken down by season.

4. Back Trajectory and Collocated Satellite Analysis

As described in section 2.3, three-dimensional Lagrangian back trajectories are produced for each 6 h period during the deployment. MODIS cloud LWP and N_d estimates are associated with these trajectories (see section 2.4), and composites for low-CCN events and non-low-CCN events are produced as a function of time prior to the trajectory arrival at Graciosa. Because the Terra and Aqua overpass times are quite close, we average trajectory-associated data from Terra and Aqua during the same day.

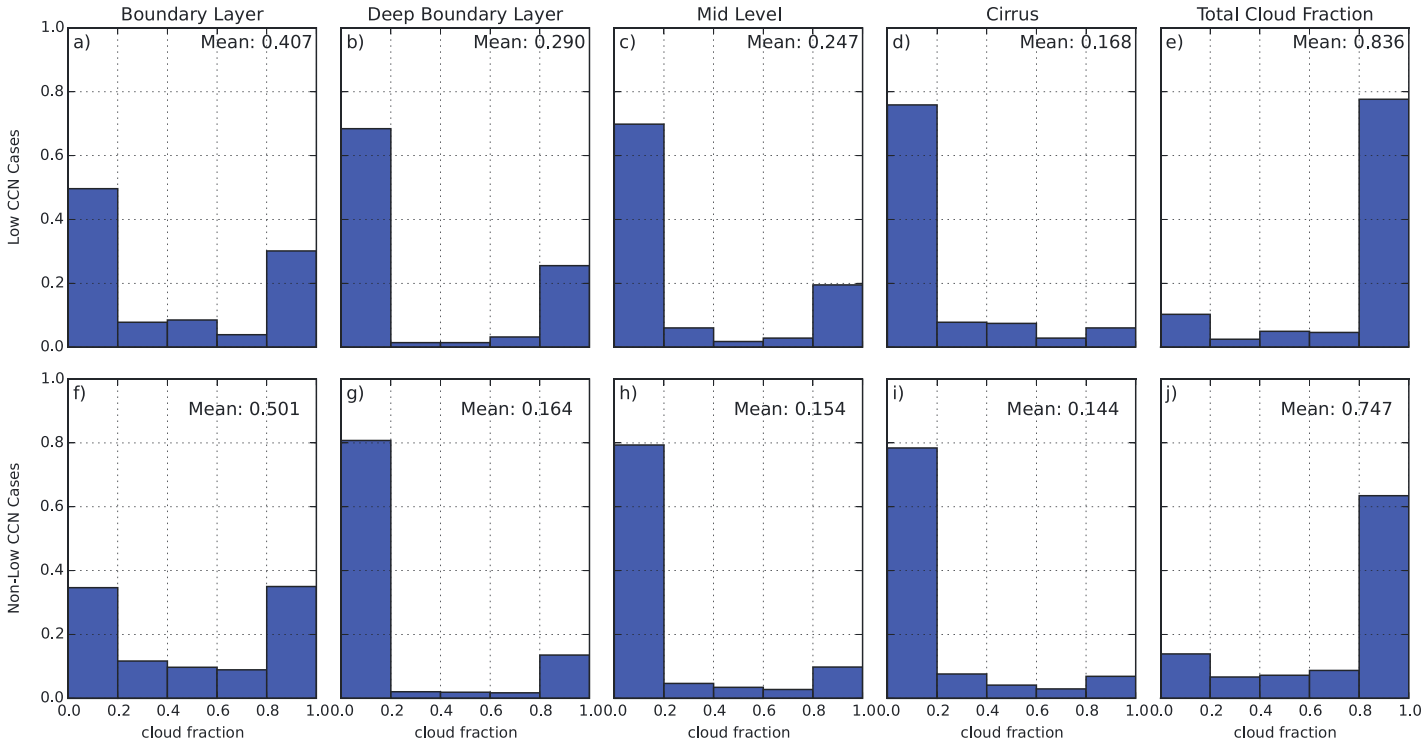

Figure 10. Cloud fraction histograms for different cloud types and total cloud fraction (a–e) during low-CCN events and (f–j) for non-low-CCN cases. The cloud types are from *Rémillard et al.* [2012] and are described in section 2.1.2. Each panel also shows the fraction of each cloud type observed. Note that the sum of cloud fractions over each type is greater than the overall cloud fraction because more than one cloud type can be present at the same time.

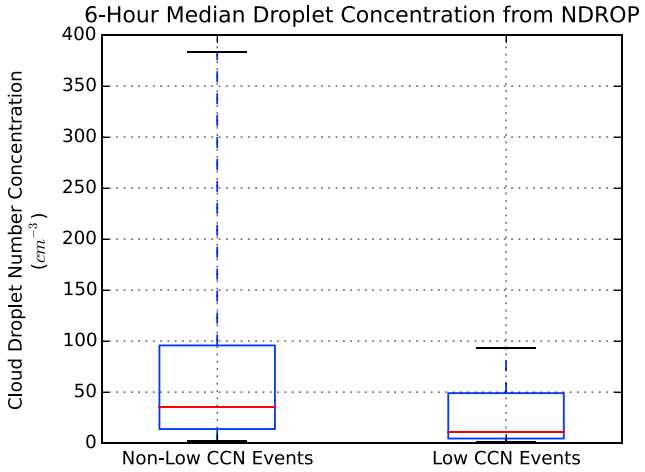

Figure 11. Box-whisker plots showing the distribution of 6 h median surface-derived N_d measurements at Graciosa for the (left) non-low and (right) low-CCN events during the entire deployment. Boxes show 25th, 50th (red line), and 75th percentiles, and whiskers reach out to show the 5th and 95th percentiles.

Before examining satellite composites, we first show trajectories ending at Graciosa overlaid on MSLP maps at the start of all low-CCN events (Figure 12). Many, but not all, of the events have a significant zonal (westerly) component, consistent with the evolution of MSLP discussed in section 3.2 (Figure 7). Many trajectories move off the North American continent and pass over the Labrador Sea area, and as many of these cases occur during the winter and spring, one would expect many of them to be associated with cold air outbreaks. This is indeed borne out with MCAO index (μ, equation (1)) statistics. To assess whether a given back trajectory passes through a cold air outbreak region at some point, we take the upper 90th percentile of μ along each trajectory, and then examine histograms of this 90th percentile value for low-CCN events and other cases. Taking simply the maximum value produces similar results. Values of μ close to zero are indicative of cold air outbreaks over water, and these are more than twice as commonly seen along low-CCN event back trajectories than in other cases (Figure 13). Not all low-CCN event back trajectories are associated with cold air outbreaks, and so it is important to not overstate the importance of cold air outbreaks, yet there is an interesting association that warrants closer inspection.

The composite evolution of N_d for air masses reaching Graciosa during low-CCN events is contrasted with the behavior for non-low-CCN cases (Figure 14), showing that the N_d distributions during low-CCN events differ quite strongly in the few days running up to the trajectory arrival at Graciosa (rightmost green bars in Figure 14). Lower N_d values are expected during low-CCN events because previous observations have demonstrated that N_d in the MBL is limited by CCN availability, particularly under low-CCN conditions [e.g., *Martin et al.*, 1994; *Ramanathan*, 2001; *Hudson et al.*, 2010; *Painemal and Zuidema*, 2013]. In the non-low-CCN trajectory ensemble, the 50th percentile of N_d values in the 24 h period prior to arrival at Graciosa is 50 cm^{-3}, but it is 25 cm^{-3} for the low-CCN cases, with each N_d distribution shifted to lower values. What is perhaps surprising is that these differences in the N_d distributions are in place up to 4 days prior to arrival at Graciosa. Prior to 4 days, the distributions become more alike and are statistically indistinguishable. In other words, the divergence in N_d distributions begins several days prior to arrival at Graciosa. This finding generally supports the idea that the processes controlling the formation of low-CCN events are generally not local to Graciosa, but appear to be set in play by events occurring several days earlier. It is also interesting to note that the time evolution of N_d over the 4 days prior to arrival shows that N_d is decreasing for both low-CCN event trajectories and non-low-CCN cases (Figure 14), suggesting that there is a general reduction of N_d regardless of whether a trajectory becomes a low-CCN event or not. We discuss this further in section 5.

To gain further insight into the divergence of N_d distributions for low-CCN events over the days prior to arrival at Graciosa, Figure 15 shows the corresponding time evolution of cloud LWP (for liquid clouds) along the trajectories. Consistent with there being little difference in LWP distributions observed at Graciosa between low-CCN and non-low-CCN events (Figure 9), the MODIS-derived LWP values in the 24 h prior to trajectory arrival at Graciosa also show little difference (Figure 15). However, 2–4 days before arrival, LWPs for low-CCN

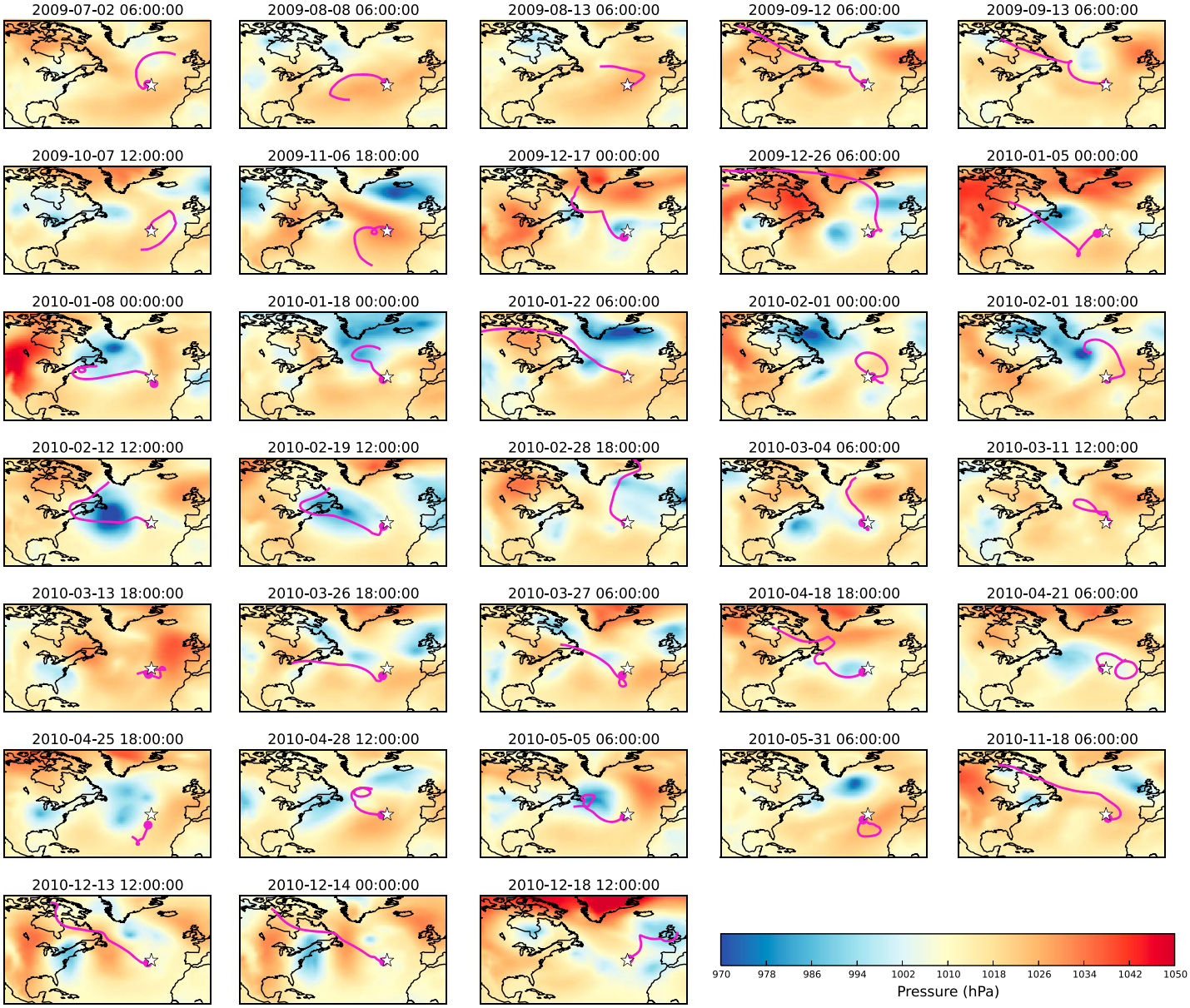

Figure 12. Maps of MSLP (colors) for all low-CCN events at Graciosa (star) at the event start time, with their respective 148 h back trajectories overlaid.

events tend to be ~30% greater than those for non-low-CCN cases. These high LWP values occur as the relative divergence in N_d distributions ((non-low minus low)/non-low) is increasing from ~0.3 to >0.4 (Figure 14).

Examination of the individual back trajectories reveals that several low-CCN event trajectories are associated with either marine or continental cold air outbreaks (Figure 12). An example of such a case can be seen in Figure 16. This particular event encapsulates several of the typical features seen for low-CCN events determined in previous sections. First, the trajectory shows southerly flow as the air mass reaches the Graciosa (Figure 16, right column), consistent with surface wind data (Figure 6). Second, a low pressure center is located to the west of Graciosa at this time, consistent with the average behavior for low-CCN events (Figure 7). The low-pressure cyclonic system results in a turning of the winds to southerly during the final few hours prior to arrival at Graciosa. Prior to this, the trajectory spends 4 days moving from the north and west (see Figure 16, middle column) as part of a cold air outbreak emerging over the Labrador Sea between Greenland and Canada, as indicated by the MCAO index (section 2.2), which is positive (Figures 16, left column and 16, middle column). Between 13 and 15 December, i.e., 2–4 days prior to arrival at Graciosa, the cloud field at the trajectory location changes from overcast shallow stratocumulus clouds that extend over a broad region

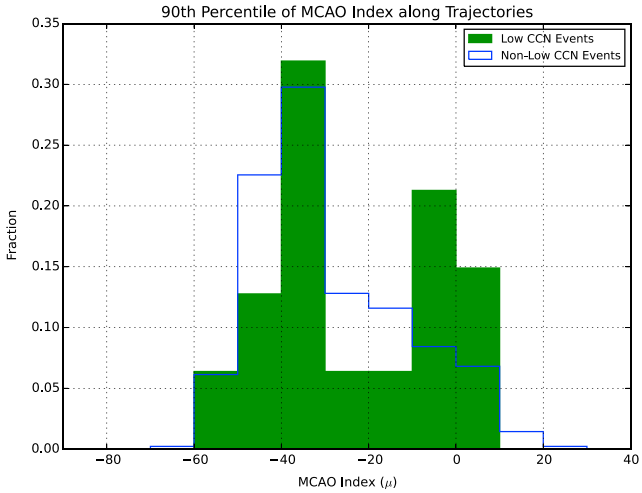

Figure 13. Trajectories resulting in low-CCN events at Graciosa tend to have encountered cold air outbreaks more frequently. Figure shows histograms of the upper 90th percentile of the MCAO index (μ, see equation (1)) along each back trajectory, for low-CCN cases (solid green) and for non-low-CCN cases (open blue).

to the east of Labrador to open mesoscale cellular convection. Observations and modeling have shown that transitions from closed to open cellular convection in the tropics/subtropics are driven by strong drizzle that reaches the surface [*Mechem and Kogan*, 2003; *Stevens et al.*, 2005; *Savic-Jovcic and Stevens*, 2008; *Wang and Feingold*, 2009] and are associated with large depletions of CCN through coalescence scavenging [*Sharon et al.*, 2006; *Terai et al.*, 2014; *Wang et al.*, 2010; *Wood et al.*, 2011; *Berner et al.*, 2013]. In midlatitude cold air outbreaks, similarly high LWP and low N_d are found [*Field et al.*, 2014], suggesting that similar processes may be working to deplete CCN.

5. Mechanisms for CCN Depletion

Based on the various observations presented above, it is clear that an explanation of the mechanisms behind low-CCN events at Graciosa requires understanding the evolution of the boundary layer aerosol budget in air

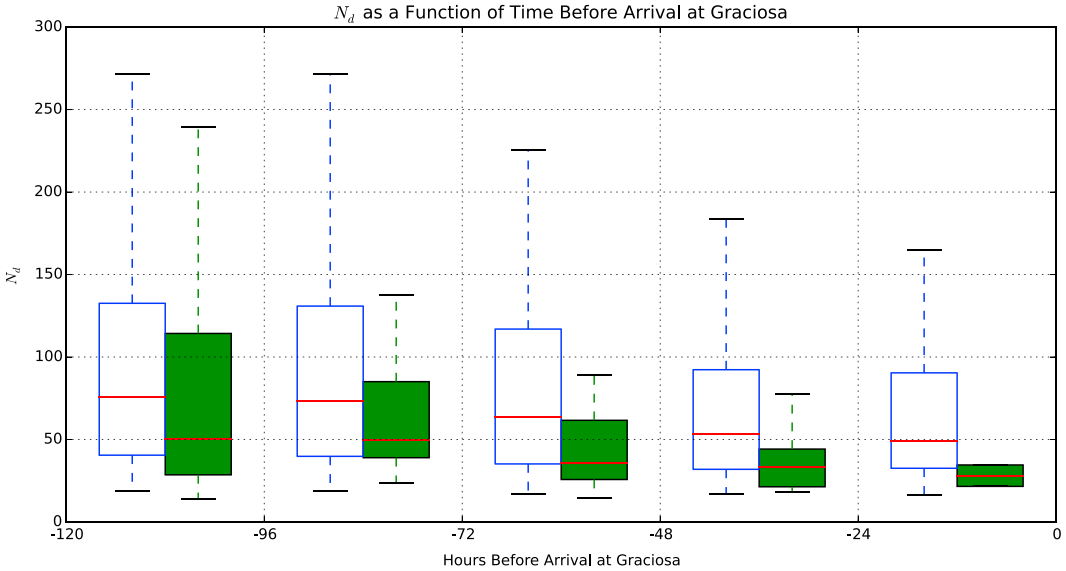

Figure 14. Composite behavior of MODIS-derived cloud droplet number concentration N_d taken from the ensemble of low-CCN (solid green box-whiskers) and non-low-CCN cases (open blue box-whiskers) as a function of time before reaching Graciosa. Box-whiskers show 25th, 50th, 75th percentiles (box), and 5th/95th percentiles of N_d (whiskers) from all the collocated satellite overpasses crossing the back trajectories. Fractional reductions of N_d for low-CCN events compared with non-low-CCN cases are 0.32, 0.33, 0.35, 0.40, and 0.46, respectively, for the 5 days prior to arrival.

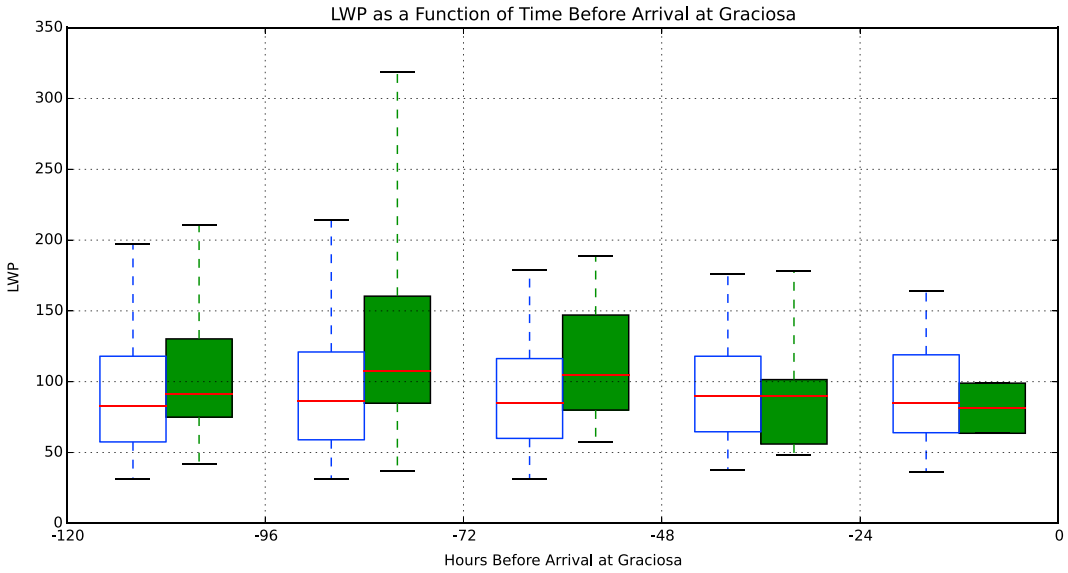

Figure 15. Composite behavior of MODIS-derived cloud LWP taken from the ensemble of low-CCN (solid green box-whiskers) and non-low-CCN cases (open blue box-whiskers) as a function of time before reaching Graciosa. Box-whiskers show 25th, 50th, 75th percentiles (box), and 5th/95th percentiles of N_d (whiskers) from all the collocated satellite overpasses crossing the back trajectories.

masses over several days prior to arriving at the island. In this section, we explore possible mechanisms to help explain the low-CCN events. Quantifying terms in the CCN budget is challenging because of the complexity of aerosol sources and sinks in the MBL [*Fitzgerald*, 1991; *O'Dowd et al.*, 1997; *Quinn and Bates*, 2011; *Hudson et al.*, 2015]. Nevertheless, we are able to use observations here to estimate some of the key source and sink terms.

5.1. Aerosol Sinks

CCN in the MBL are lost through precipitation processes and through dry deposition, the latter of which has been shown to be generally much smaller than the former [*Wood et al.*, 2012]. In the cloudy MBL, and especially during the transition from closed to open mesoscale cellular convection, coalescence scavenging is the dominant CCN sink [*Berner et al.*, 2013]. We focus first on the shift in the N_d distributions to lower values several days upstream of Graciosa (Figure 14) and ask if this divergence can be caused by the higher values of LWP at that time. We focus on the period 48–96 h prior to trajectory arrival at Graciosa and use the expression for loss rates discussed above in the introduction that relates MBL-averaged CCN loss rates to cloud thickness [*Wood*, 2006, equation (18)]. Assuming an adiabatic relationship between cloud thickness and LWP [*Albrecht et al.*, 1990], we use a cloud top temperature of 275 K and pressure of 850 hPa to estimate the adiabatic increase of LWC with altitude in cloud. We also assume an MBL depth of 1500 m consistent with mean values over midlatitude oceans [*Rémillard et al.*, 2012; *Chan and Wood*, 2013]. The low-CCN trajectory set has a median LWP (MODIS) that is approximately 20–30% higher than that for non-low-CCN cases (Figure 15), but the more skewed LWP distribution to higher values may also be important. To address this, we use the entire LWP distribution in Figure 15 for 48–96 h prior to arrival at Graciosa to estimate the mean MBL CCN loss rates and find that for the low-CCN trajectory set the mean loss rate is 55 cm^{-3} d^{-1} compared to 35 cm^{-3} d^{-1} for the non-low-CCN set. Loss rates for other composite trajectory days are not markedly different for low and non-low-CCN events and are in the range 30–40 cm^{-3} d^{-1}.

Assuming that the difference of ~20 cm^{-3} d^{-1} in the mean loss rates for low and non-low-CCN trajectories is applicable to the entire 2 day period and that source rates are similar for the two trajectory sets, we can estimate that it would cause the mean N_d values for the low-CCN event trajectories to be reduced by several tens of cm^{-3} compared with the non-low-CCN trajectories. Indeed, Figure 14 does show that a differential of this magnitude is evident in the N_d distributions during and after this period. Although this calculation is not definitive, it does hint at possible cause of removal of CCN from coalescence scavenging in anomalously thick liquid clouds that are associated with cold air outbreaks.

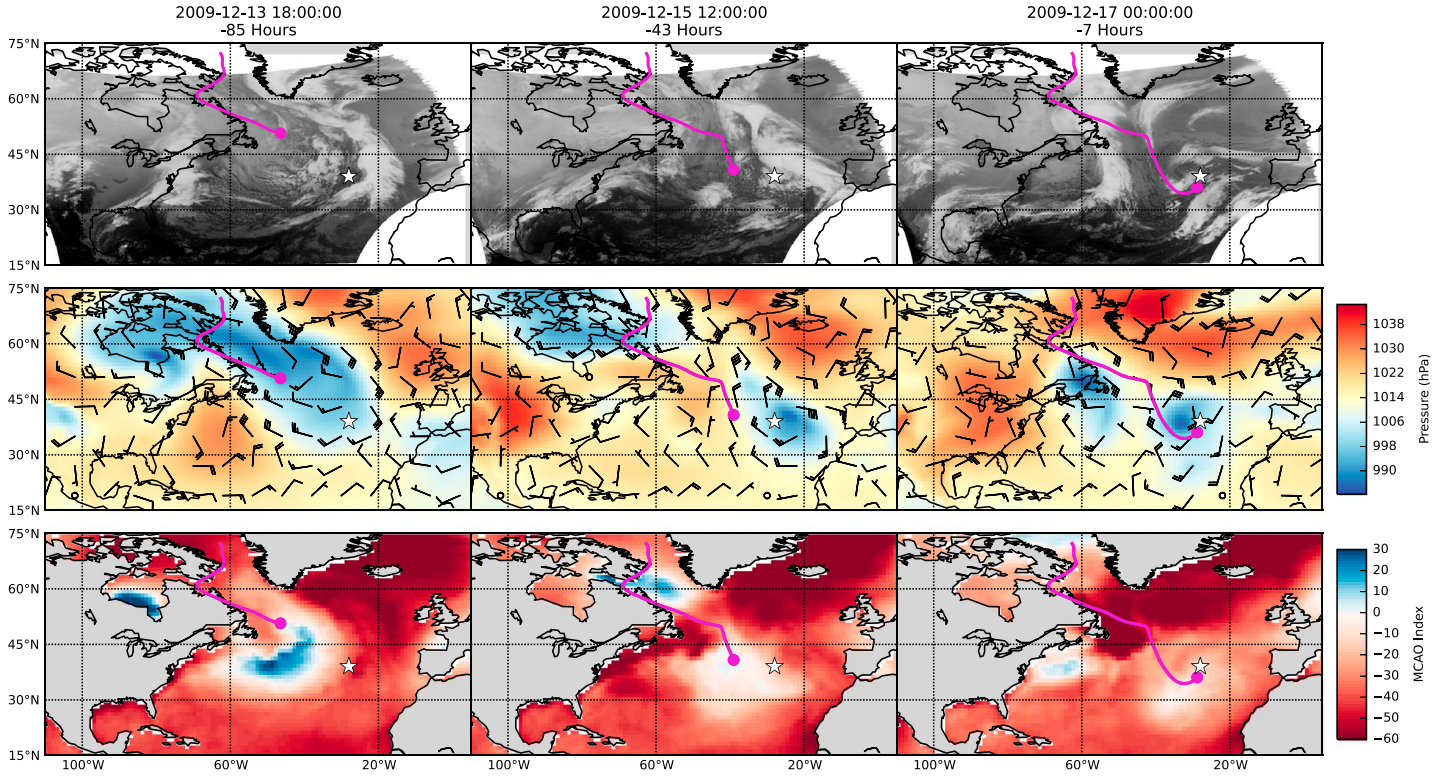

Figure 16. (top row) Evolution of cloud (thermal infrared GOES imagery with light colors representing cold clouds), (middle row) mean sea level pressure and wind barbs (knots for wind speeds using standard meteorological convention), and (bottom row) a marine cold air outbreak (MCAO) index (with values close to zero and above indicative of cold air outbreaks, see text) for a cold air outbreak case resulting in a low-CCN event at Graciosa on 17 December 2009 that lasted from 00 UTC to 12 UTC. The panels show data at (left column) 85, (middle column) 43, and (right column) 7 h prior to trajectory arrival during the middle of the low-CCN event at Graciosa. The trajectory is shown in each panel, with the circle at its end location at the corresponding time.

5.2. Aerosol Sources

Two of the main aerosol sources in the MBL are (a) particles derived from the ocean and (b) entrainment of particles from the free troposphere [*Capaldo et al.*, 1999; *Katoshevski et al.*, 1999; *Clarke et al.*, 2006; *Wood et al.*, 2012; *Clarke et al.*, 2013]. New particle formation in the MBL is thought to be less important overall, although there appear to be occasions where it does occur [*Tomlinson et al.*, 2007], and modeling work suggests the possibility of new particle formation constituting a significant source of CCN during conditions of ultralow CCN [*Kazil et al.*, 2011] in pockets of open cells. We have no means to estimate the rate of new CCN production from new particle formation, but sea spray particle formation is wind speed dependent and can be estimated using previously published formulations. Aqueous phase cloud processing within the MBL can also grow particles, decreasing their critical supersaturation and effectively serving as a source of CCN at low S [e.g., *Hudson et al.*, 2015], but the rate at which this occurs is contingent on the availability of sulfate (and possibly organic) sources and is difficult to model in a simple framework.

The entrainment rate of air from the free troposphere (FT) depends upon many factors [see, e.g., *Wood*, 2012; *Clarke et al.*, 2013]. An estimate of entrainment rate can be made using energy, moisture and mass budgets [e.g., *Caldwell et al.*, 2005], but satellite observations show that over broad areas of the subtropical and tropical ocean, the mean entrainment rate only exceeds the mean subsidence rate by ~30% [*Wood and Bretherton*, 2004], so reanalysis estimates of subsidence rate should yield an estimate of the entrainment rate better than a factor of 2, and this approach was used in *Wood et al.* [2012] to successfully predict N_d gradients over the southeastern Pacific. We make the same assumption here to estimate mean entrainment rate for the trajectory groups. Mean subsidence rates along the low-CCN and non-low-CCN trajectories are found to be similar (not shown) and are 2.0–2.5 mm s^{-1}. More uncertain is the concentration of CCN-sized particles in the FT. In the subtropical and tropical regions, there is sufficient residence time in the FT from new particle formation in the deep convective detrainment regions of the upper troposphere to allow the establishment of quasi self-preserving aerosol distributions, and this may limit the spatial and temporal variability of the aerosol size

distribution by the time parcels reach the lower FT [*Raes*, 1995]. In the midlatitudes, however, the sources of FT particles are not as well quantified or understood. Summertime FT N_{CCN} at $S = 0.2\%$, measured in the vicinity of the Azores are close to 100 cm^{-3} [*Hudson and Xie*, 1999], which is similar to FT values over the remote southeastern Pacific [*Allen et al.*, 2011], with values at $S = 0.1\%$ expected to be slightly lower than this. Such values are higher than MBL CCN concentrations at Graciosa during low-CCN events (Figure 2) but similar to concentrations at other times, implying that entrainment from the FT is likely weakly buffering CCN losses from coalescence scavenging. Calculations of the replenishment rate from entrainment [see, e.g., *Wood et al.*, 2012] indicate an upper limit for the buffering of CCN from FT entrainment of approximately 10–15 cm^{-3} d^{-1} in the case that the MBL contains no CCN at all. In actual fact, mean CCN and N_d for both low-CCN events and non-low cases (e.g., Figure 14) are well above zero, so we estimate mean replenishment rates from entrainment to be 5–10 cm^{-3} d^{-1} for low-CCN events and <5 cm^{-3} d^{-1} for non-low-CCN cases.

The other key aerosol source in the PBL is from sea spray production, which is surface wind speed dependent. We use the approach taken in *Wood et al.* [2012] to estimate surface sea spray production rates based on *Clarke et al.* [2006] and surface wind speeds taken from reanalysis data interpolated in time and space onto the HYSPLIT back trajectories. CCN fluxes at $S = 0.1\%$ are estimated assuming that emitted particles are sodium chloride. Based on this, we obtain a CCN flux rate equal to $\dot{N}_{CCN,0.1\%} = F u_{10}^{3.41}/z_i$ where u_{10} is the wind speed at an altitude of 10 m, z_i is the PBL depth, and F is an S-dependent function. Based on Figure 1 in *Wood et al.* [2012], $F = 132\ m^{-3}(m\ s^{-1})^{-2.41}$. As before, we assume $z_i = 1500$ m, so that $\dot{N}_{CCN,0.1\%} \approx 2$, 20, and 80 cm^{-3} d^{-1} for $u_{10} = 5$, 10 and 15 m s^{-1}, respectively. As with the loss rates, we use the PDF of surface wind speeds along the trajectories to estimate mean CCN sea spray source rates. During the period 48–96 h prior to arrival at Graciosa, the mean surface values of $\dot{N}_{CCN,0.1\%}$ are estimated to be 15–20 cm^{-3} d^{-1} with very little difference between rates for low-CCN and non-low trajectories. A key implication of this is that differences in aerosol sources are not likely to be responsible for the differential in N_{CCN} (and N_d) between low-CCN events and non-low-CCN cases.

5.3. Implications for Overall CCN Budget

For non-low-CCN events, the calculations in the previous two subsections for the time period 48–96 h prior to air mass arrival at Graciosa suggest surface sea spray sources of 15–20 cm^{-3} d^{-1}, with the mean source rate from FT entrainment of <5 cm^{-3} d^{-1}, and precipitation losses of ~35 cm^{-3} d^{-1}. Assuming these are the primary terms in the CCN budget, it is reasonable to expect that there would be a slow decline (~10–15 cm^{-3} d^{-1}) in N_{CCN} and N_d over this period. Indeed, this is supported by observations (Figure 14), where median N_d falls by ≈25 cm^{-3} from 96 to 48 h before arrival. For the low-CCN events, sea spray source rates are estimated to be similar to those for non-low-CCN cases (15–20 cm^{-3} d^{-1}), but the sink rate is closer to 55 cm^{-3} d^{-1}, and the FT aerosol source is likely to be ~5–10 cm^{-3} d^{-1} because of the greater differential between the concentration in the FT and the MBL. Thus, for low-CCN events during 48–96 h prior to arrival, we might expect mean overall CCN loss rates of perhaps 25–35 cm^{-3} d^{-1}, or approximately double those for non-low-CCN cases. Thus, we postulate that low-CCN events are driven by stronger coalescence scavenging in high LWP clouds associated with cold air outbreaks ~2–4 days upstream of Graciosa.

6. Conceptual Model

In this paper, we have identified a connection between cold air outbreak events and subsequent very low-CCN concentrations at Graciosa. Not all low-CCN events can be explained in this way, but a significant number of them can, and so we present Figure 17 as a canonical case and as a means to introduce a conceptual model to explain how low N_{CCN} in cold air outbreaks are created. Essentially, a deep surface low over the northern North Atlantic (see Figure 16, left column) moves cold continental and/or polar maritime air from the north and west over the warmer surface waters of the North Atlantic. The strong surface fluxes encountered as the cold air streams over warmer waters result initially in overcast stratocumulus clouds in a shallow PBL. Strong surface driving and also cloud top longwave cooling helps drive turbulent entrainment that rapidly deepens the PBL, resulting in cloud thickening and corresponding LWP increases. In the case shown in Figure 17, there is a large region over which the LWP exceeds 500 g m^{-2}, which would remove CCN through coalescence scavenging at a rate of roughly 500 cm^{-3} d^{-1} according to the model used in section 5.1. In the trajectory ensemble mean, loss rates via coalescence scavenging are clearly lower than this, but we demonstrate that the mean loss rates are considerably higher for low-CCN events because these trajectories encounter clouds with higher LWP.

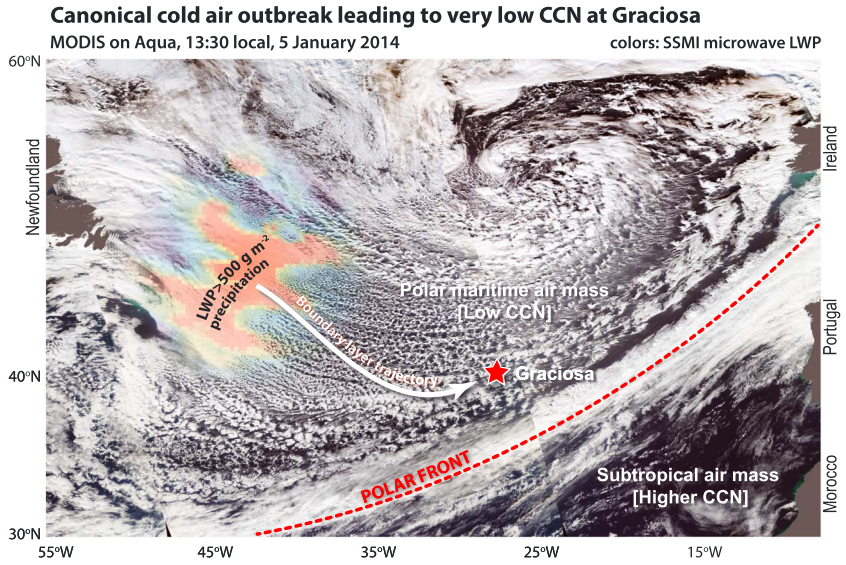

Figure 17. Canonical cold air outbreak case motivating a conceptual model of how precipitating boundary layer clouds can produce very low CCN concentrations at Graciosa. The main image shows a composite of RGB visible imagery from three MODIS swaths from the NASA Aqua satellite (~13:30 h local overpass time) on 5 January 2014 over the North Atlantic. High liquid water path, shown using LWP retrieved earlier that day (06 h local) from the passive microwave Special Sensor Microwave Imager (SSMI) instrument on the F17 Defense Meteorological Satellite, is found over a broad area (red colors indicate LWP in excess of 500 g m^{-2}) prior to the marine stratocumulus cloud breakup into open cells. In this case, trajectories flowing over Graciosa passed through the region of high LWP 1–2 days prior to arrival. Often, the location of the polar front (red dashed line) delineates the boundary between the very low-CCN cold, polar flow from the more CCN-rich subtropical air mass.

The conceptual model encapsulated in Figure 17, and particularly the spatial extent of the cold air outbreak open cell clouds, suggests that basin-scale CCN variability may be induced by cold air outbreaks and that more attention should be paid to the causes of CCN variability in the midlatitude marine PBL.

7. Conclusions

In this study, we examine aerosol, cloud and meteorological characteristics of very low-CCN events (6 h mean N_{CCN} at $S = 0.1\%$ below 20 cm^{-3}) occurring at Graciosa Island in the eastern North Atlantic. The various findings from this study were used to propose a conceptual model to explain the occurrence of very low N_{CCN} in the remote MBL. Table 2 summarizes the key meteorological aspects that differentiate low-CCN events from non-low-CCN conditions. The association of a number of the low-CCN events with cold air outbreak conditions upstream is particularly interesting and important, and examining the seasonality of cold air outbreak events may help to explain the apparent seasonal preference for low-CCN events during winter and spring. *Kolstad et al.* [2009] examined the seasonal cycle of the MCAO index (equation (1)) over a broad region of the NW Atlantic including the Labrador Sea over which a number of the low-CCN event trajectories passed and found maximum values from December to March, with the seasonality largely driven by colder 700 hPa temperatures during these months. Our analysis of the MCAO index along the back trajectories arriving at Graciosa (Figure 13) shows that low-CCN event back trajectories are approximately twice as likely to have encountered a cold air outbreak compared to other cases.

We find that N_d are lower at Graciosa during low-CCN events than at other times, but that the reductions in N_d that lead to these differences happen several days upstream of Graciosa, often during cold air outbreaks, where coincident LWP values are anomalously large. Based on this, it is hypothesized here that coalescence scavenging of cloud droplets during precipitation formation under high LWP conditions associated with cold air outbreaks may be partly responsible for the shift of the low-CCN event N_d distribution to smaller values in trajectories that constitute low-CCN events. We hope that our findings and conceptual model can inform further study of factors controlling aerosol variability at the Azores and over the remote subtropical and midlatitude oceans in general.

Table 2. Distinguishing Characteristics of Low-CCN Events

Characteristic	Low-CCN Events	Non-Low-CCN Conditions
Seasonality	Three quarters of events during DJF and MAM	Occur all year round
CCN concentrations (0.1%)	Median 15 cm^{-3}; 90% from 5 to 25 cm^{-3}	median 80 cm^{-3}; 90% from 25 to 215 cm^{-3}
Aerosol scattering	Low values (both submicron and total) suppressed in approximate proportion to $N_{CCN,0.1\%}$	Larger and more variable scattering
Wind direction (10 m) at Graciosa	Most cases from SW through SE.	Wide range of directions, many from SW clockwise through NW
Wind speed (10 m) at Graciosa	Median wind speed 3 m s^{-1}	Median wind speed 5 m s^{-1}
Back trajectory history	More trajectories experiencing cold air outbreak conditions	Fewer cold air outbreak encounters
Cloud droplet concentration N_d	20–50% lower N_d beginning several days upstream	Higher N_d beginning several days upstream
Liquid water path (LWP)	Little difference at Graciosa but large values 2–3 days prior to trajectory arrival at Graciosa	Little difference at Graciosa; upstream distributions flat.

Appendix A: Corrections to CCN Counter

As mentioned in section 2.1.1, the CCN measurements were found to be problematic for October 2009 to June 2010, and a flow rate correction is described here that uses the CN counter as a reference instrument. Köhler calculations indicate that a supersaturation S of approximately 1% should be sufficient to activate most soluble particles larger than 20 nm in diameter. Remote marine regions away from sources of significant new particle formation, observations indicate relatively few particles in the size range 10–20 nm [*Heintzenberg et al.*, 2000; *Allen et al.*, 2011]. Therefore, we would expect N_{CCN} measured at $S \approx 1\%$ to be close to the concentrations from the CN counter. At the beginning of the record (April–September 2009) and after the cleaning (July–December 2010), this is quite close to what we observe, although the CN counter monthly mean concentrations tend to be approximately 20% below those from the CCN counter at $S = 1.11\%$ (Figure 1a). Other than during the problematic period (Oct 2009 to June 2010), the ratio of CN to CCN at $S = 1.11\%$ is stable (compare periods before and after the degraded period in Figure 1a), suggesting that either the CCN counter or CN counter has a stable systematic bias in measured concentration. In this study, we assume that the CN counter is correct, although assuming the reverse has no significant impact upon the primary conclusions of this study.

Importantly, we note that the degradation in concentrations from October 2009 to June 2010 is seen in all channels (Figure 1). The ratio of N_{CCN} measured at any two supersaturations is stable and shows no sign of changing during the degradation period (not shown). For example, the ratio of N_{CCN} at 0.1% to that at 1.11% is 0.19 (with the month to month standard deviation of this ratio of 0.04) during the months of good counter operation, and 0.17 (SD 0.04) during the degraded months. This indicates that the degradation is affecting concentrations at all S in the same way, and that a single sample volume correction for one S can be applied to all S. We apply this correction on a monthly basis by multiplying the monthly mean CCN at $S = 1.11\%$ to ensure equality with the monthly mean N_{CN} (with high variance measurements removed as discussed in the caption for (Figure 1). The monthly multiplication factors are then applied to concentrations at all supersaturations during the month. Corrected N_{CCN} is shown in Figure 1b. Although we have no independent means to verify the accuracy of the corrected concentrations, we note that the seasonal cycle of submicron aerosol scattering coefficient at 450 nm wavelength tracks quite well the concentrations of particles at the lower S (Figure 1b). Corrected N_{CCN} are used exclusively in this study.

Acknowledgments
The CAP-MBL deployment of the ARM Mobile Facility was supported by the U.S. Department of Energy (DOE) Atmospheric Radiation Measurement (ARM) Program Climate Research Facility and the DOE Atmospheric Sciences Program. We are indebted to the scientists and staff who made this work possible by taking and quality controlling the measurements. Data were obtained from the ARM program archive, sponsored by DOE, Office of Science, Office of Biological and Environmental Research Environmental Science Division. This work was supported by DOE grants DE SC0006865MOD0002 and DE-SC0013489 (PI Robert Wood). MODIS data were obtained from the NASA Goddard Land Processes data archive, GOES data from the NOAA CLASS website, and SSM/I data from Remote Sensing Systems (data from http://www.remss.com). ERA-Interim data are provided by the European Center for Medium Range Weather Forecasts (ECMWF). The HYSPLIT IV model was obtained from the NOAA Air Resources Laboratory.

References

Albrecht, B. A., C. W. Fairall, D. W. Thomson, A. B. White, J. B. Snider, and W. H. Schubert (1990), Surface-based remote sensing of the observed and the adiabatic liquid water content of stratocumulus clouds, *Geophys. Res. Lett.*, *17*(1), 89–92, doi:10.1029/GL017i001p00089.

Allen, G., et al. (2011), South East Pacific atmospheric composition and variability sampled along 20°S during VOCALS-REx, *Atmos. Chem. Phys.*, *11*(11), 5237–5262, doi:10.5194/acp-11-5237-2011.

Andreae, M. O. (2007), Aerosols before pollution, *Science*, *315*(5808), 50–51, doi:10.1126/science.1136529.
Baker, M. B., and R. J. Charlson (1990), Bistability of CCN concentrations and thermodynamics in the cloud-topped boundary layer, *Nature*, *345*(6271), 142–145, doi:10.1038/345142a0.
Bennartz, R. (2007), Global assessment of marine boundary layer cloud droplet number concentration from satellite, *J. Geophys. Res.*, *112*, D02201, doi:10.1029/2006JD007547.
Berner, A. H., C. S. Bretherton, R. Wood, and A. Muhlbauer (2013), Marine boundary layer cloud regimes and POC formation in a CRM coupled to a bulk aerosol scheme, *Atmos. Chem. Phys.*, *13*(24), 12,549–12,572, doi:10.5194/acp-13-12549-2013.
Boers, R., and R. M. Mitchell (1994), Absorption feedback in stratocumulus clouds influence on cloud top albedo, *Tellus A*, *46*(3), 229–241, doi:10.1034/j.1600-0870.1994.00001.x.
Boers, R., J. B. Jensen, and P. B. Krummel (1998), Microphysical and short-wave radiative structure of stratocumulus clouds over the Southern Ocean: Summer results and seasonal differences, *Q. J. R. Meteorol. Soc.*, *124*(545), 151–168.
Boers, R., J. R. Acarreta, and J. L. Gras (2006), Satellite monitoring of the first indirect aerosol effect: Retrieval of the droplet concentration of water clouds, *J. Geophys. Res.*, *111*, D2220, doi:10.1029/2005JD006838.
Caldwell, P., C. S. Bretherton, and R. Wood (2005), Mixed-layer budget analysis of the diurnal cycle of entrainment in southeast Pacific stratocumulus, *J. Atmos. Sci.*, *62*(10), 3775–3791.
Capaldo, K. P., P. Kasibhatla, and S. N. Pandis (1999), Is aerosol production within the remote marine boundary layer sufficient to maintain observed concentrations?, *J. Geophys. Res.*, *104*(D3), 3483–3500, doi:10.1029/1998JD100080.
Carslaw, K. S., et al. (2013), Large contribution of natural aerosols to uncertainty in indirect forcing, *Nature*, *503*(7474), 67–71, doi:10.1038/nature12674.
Chan, K. M., and R. Wood (2013), The seasonal cycle of planetary boundary layer depth determined using COSMIC radio occultation data: Seasonal cycle of PBL depth, *J. Geophys. Res. Atmos.*, *118*, 12,422–12,434, doi:10.1002/2013JD020147.
Clarke, A. D., S. R. Owens, and J. Zhou (2006), An ultrafine sea-salt flux from breaking waves: Implications for cloud condensation nuclei in the remote marine atmosphere, *J. Geophys. Res.*, *111*, D06202, doi:10.1029/2005JD006565.
Clarke, A. D., S. Freitag, R. M. C. Simpson, J. G. Hudson, S. G. Howell, V. L. Brekhovskikh, T. Campos, V. N. Kapustin, and J. Zhou (2013), Free troposphere as a major source of CCN for the equatorial Pacific boundary layer: Long-range transport and teleconnections, *Atmos. Chem. Phys.*, *13*(15), 7511–7529, doi:10.5194/acp-13-7511-2013.
Comstock, K. K., R. Wood, S. E. Yuter, and C. S. Bretherton (2004), Reflectivity and rain rate in and below drizzling stratocumulus, *Q. J. R. Meteorol. Soc.*, *130*(603), 2891–2918, doi:10.1256/qj.03.187.
Dee, D. P., et al. (2011), The ERA-Interim reanalysis: Configuration and performance of the data assimilation system, *Q. J. R. Meteorol. Soc.*, *137*(656), 553–597, doi:10.1002/qj.828.
Draxier, R., and G. Hess (1998), An overview of the HYSPLIT_4 modelling system for trajectories, dispersion and deposition, *Aust. Meteorol. Mag.*, *47*(4), 295–308.
Feingold, G., S. M. Kreidenweis, B. Stevens, and W. R. Cotton (1996), Numerical simulations of stratocumulus processing of cloud condensation nuclei through collision-coalescence, *J. Geophys. Res.*, *101*(D16), 21,391–21,402, doi:10.1029/96JD01552.
Field, P. R., R. J. Cotton, K. McBeath, A. P. Lock, S. Webster, and R. P. Allan (2014), Improving a convection-permitting model simulation of a cold air outbreak, *Q. J. R. Meteorol. Soc.*, *140*(678), 124–138, doi:10.1002/qj.2116.
Fitzgerald, J. W. (1991), Marine aerosols: A review, *Atmos. Environ. Part A*, *25*(3–4), 533–545, doi:10.1016/0960-1686(91)90050-H.
Ghan, S. J., S. J. Smith, M. Wang, K. Zhang, K. Pringle, K. Carslaw, J. Pierce, S. Bauer, and P. Adams (2013), A simple model of global aerosol indirect effects: Global aerosol indirect effects, *J. Geophys. Res. Atmos.*, *118*, 6688–6707, doi:10.1002/jgrd.50567.
Goren, T., and D. Rosenfeld (2015), Extensive closed cell marine stratocumulus downwind of Europe—A large aerosol cloud mediated radiative effect or forcing?, *J. Geophys. Res. Atmos.*, *120*, 6098–6116, doi:10.1002/2015JD023176.
Grosvenor, D. P., and R. Wood (2014), The effect of solar zenith angle on MODIS cloud optical and microphysical retrievals within marine liquid water clouds, *Atmos. Chem. Phys.*, *14*(14), 7291–7321, doi:10.5194/acp-14-7291-2014.
Hamilton, D. S., L. A. Lee, K. J. Pringle, C. L. Reddington, D. V. Spracklen, and K. S. Carslaw (2014), Occurrence of pristine aerosol environments on a polluted planet, *Proc. Natl. Acad. Sci. U.S.A.*, *111*(52), 18,466–18,471, doi:10.1073/pnas.1415440111.
Heintzenberg, J., D. C. Covert, and R. Van Dingenen (2000), Size distribution and chemical composition of marine aerosols: A compilation and review, *Tellus B*, *52*(4), 1104–1122.
Hindman, E. E., W. M. Porch, J. G. Hudson, and P. A. Durkee (1994), Ship-produced cloud lines of 13 July 1991, *Atmos. Environ.*, *28*(20), 3393–3403, doi:10.1016/1352-2310(94)00171-G.
Hudson, J. G., and S. Noble (2009), CCN and cloud droplet concentrations at a remote ocean site, *Geophys. Res. Lett.*, *36*, L13812, doi:10.1029/2009GL038465.
Hudson, J. G., and Y. Xie (1999), Vertical distributions of cloud condensation nuclei spectra over the summertime northeast Pacific and Atlantic Oceans, *J. Geophys. Res.*, *104*(D23), 30,219–30,229, doi:10.1029/1999JD900413.
Hudson, J. G., S. Noble, and V. Jha (2010), Stratus cloud supersaturations: Stratus cloud supersaturations, *Geophys. Res. Lett.*, *37*, L21813, doi:10.1029/2010GL045197.
Hudson, J. G., S. Noble, and S. Tabor (2015), Cloud supersaturations from CCN spectra Hoppel minima, *J. Geophys. Res. Atmos.*, *120*, 3436–3452, doi:10.1002/2014JD022669.
Intergovernmental Panel on Climate Change (2013), *Summary for Policymakers*, 1–30 pp., Cambridge Univ. Press, Cambridge U. K., and New York.
Isaksen, I. S. A., et al. (2009), Atmospheric composition change: Climate–Chemistry interactions, *Atmos. Environ.*, *43*(33), 5138–5192, doi:10.1016/j.atmosenv.2009.08.003.
Jefferson, A. (2010), Empirical estimates of CCN from aerosol optical properties at four remote sites, *Atmos. Chem. Phys.*, *10*(14), 6855–6861, doi:10.5194/acp-10-6855-2010.
Kalnay, E., et al. (1996), The NCEP/NCAR 40-year reanalysis project, *Bull. Am. Meteorol. Soc.*, *77*(3), 437–471, doi:10.1175/1520-0477(1996)077<0437:TNYRP>2.0.CO;2.
Katoshevski, D., A. Nenes, and J. H. Seinfeld (1999), A study of processes that govern the maintenance of aerosols in the marine boundary layer, *J. Aerosol Sci.*, *30*(4), 503–532, doi:10.1016/S0021-8502(98)00740-X.
Kazil, J., H. Wang, G. Feingold, A. D. Clarke, J. R. Snider, and A. R. Bandy (2011), Modeling chemical and aerosol processes in the transition from closed to open cells during VOCALS-REx, *Atmos. Chem. Phys.*, *11*(15), 7491–7514, doi:10.5194/acp-11-7491-2011.
King, M. D., S.-C. Tsay, S. E. Platnick, M. Wang, and K.-N. Liou (1997), *Cloud Retrieval Algorithms for Modis: Optical Thickness, Effective Particle Radius, and Thermodynamic Phase*, MODIS Algorithm Theoretical Basis Document ATBD-MOD-05, NASA, Greenbelt, Md.
Kolstad, E. W., and T. J. Bracegirdle (2007), Marine cold-air outbreaks in the future: An assessment of IPCC AR4 model results for the Northern Hemisphere, *Clim. Dyn.*, *30*(7–8), 871–885, doi:10.1007/s00382-007-0331-0.

Kolstad, E. W., T. J. Bracegirdle, and I. A. Seierstad (2009), Marine cold-air outbreaks in the North Atlantic: Temporal distribution and associations with large-scale atmospheric circulation, *Clim. Dyn.*, *33*(2–3), 187–197, doi:10.1007/s00382-008-0431-5.
Lance, S., A. Nenes, J. Medina, and J. N. Smith (2006), Mapping the operation of the DMT Continuous flow CCN counter, *Aerosol Sci. Technol.*, *40*(4), 242–254, doi:10.1080/02786820500543290.
Lewis, E. R., and S. E. Schwartz (2004), *Sea Salt Aerosol Production: Mechanisms, Methods, Measurements, and Models — A Critical Review, Geophys. Monogr. Ser.*, AGU, Washington, D. C.
Martin, G. M., D. W. Johnson, and A. Spice (1994), The measurement and parameterization of effective radius of droplets in warm stratocumulus clouds, *J. Atmos. Sci.*, *51*(13), 1823–1842, doi:10.1175/1520-0469(1994)051<1823:TMAPOE>2.0.CO;2.
Mauritsen, T., et al. (2011), An Arctic CCN-limited cloud-aerosol regime, *Atmos. Chem. Phys.*, *11*(1), 165–173, doi:10.5194/acp-11-165-2011.
McComiskey, A., G. Feingold, A. S. Frisch, D. D. Turner, M. A. Miller, J. C. Chiu, Q. Min, and J. A. Ogren (2009), An assessment of aerosol-cloud interactions in marine stratus clouds based on surface remote sensing, *J. Geophys. Res.*, *114*, D09203, doi:10.1029/2008JD011006.
Mechem, D. B., and Y. L. Kogan (2003), Simulating the transition from drizzling marine stratocumulus to boundary layer cumulus with a mesoscale model, *Mon. Weather Rev.*, *131*(10), 2342–2360, doi:10.1175/1520-0493(2003)131<2342:STTFDM>2.0.CO;2.
Mechem, D. B., P. C. Robinson, and Y. L. Kogan (2006), Processing of cloud condensation nuclei by collision-coalescence in a mesoscale model, *J. Geophys. Res.*, *111*, D18204, doi:10.1029/2006JD007183.
Miles, N. L., J. Verlinde, and E. E. Clothiaux (2000), Cloud droplet size distributions in low-level stratiform clouds, *J. Atmos. Sci.*, *57*(2), 295–311.
O'Dowd, C. D., M. H. Smith, I. E. Consterdine, and J. A. Lowe (1997), Marine aerosol, sea-salt, and the marine sulphur cycle: A short review, *Atmos. Environ.*, *31*(1), 73–80, doi:10.1016/S1352-2310(96)00106-9.
Oreopoulos, L. (2005), The impact of subsampling on MODIS level-3 statistics of cloud optical thickness and effective radius, *IEEE Trans. Geosci. Remote Sens.*, *43*(2), 366–373, doi:10.1109/TGRS.2004.841247.
Painemal, D., and P. Zuidema (2013), The first aerosol indirect effect quantified through airborne remote sensing during VOCALS-REx, *Atmos. Chem. Phys.*, *13*(2), 917–931, doi:10.5194/acp-13-917-2013.
Platnick, S., and S. Twomey (1994), Determining the susceptibility of cloud albedo to changes in droplet concentration with the advanced very high resolution radiometer, *J. Appl. Meteorol.*, *33*(3), 334–347, doi:10.1175/1520-0450(1994)033<0334:DTSOCA>2.0.CO;2.
Quinn, P. K., and T. S. Bates (2011), The case against climate regulation via oceanic phytoplankton sulphur emissions, *Nature*, *480*(7375), 51–56, doi:10.1038/nature10580.
Raes, F. (1995), Entrainment of free tropospheric aerosols as a regulating mechanism for cloud condensation nuclei in the remote marine boundary layer, *J. Geophys. Res.*, *100*(D2), 2893–2903, doi:10.1029/94JD02832.
Ramanathan, V. (2001), Aerosols, climate, and the hydrological cycle, *Science*, *294*(5549), 2119–2124, doi:10.1126/science.1064034.
Rémillard, J., P. Kollias, E. Luke, and R. Wood (2012), Marine boundary layer cloud observations in the Azores, *J. Clim.*, *25*(21), 7381–7398, doi:10.1175/JCLI-D-11-00610.1.
Riihimaki, L., S. McFarlane, and C. Sivaraman, (2014), Droplet number concentrations value-added product, US Dep. of Energy Rep., DOE/SC-ARM-TR-140, 29.
Roberts, G. C., and A. Nenes (2005), A continuous-flow streamwise thermal-gradient CCN chamber for atmospheric measurements, *Aerosol Sci. Technol.*, *39*(3), 206–221, doi:10.1080/027868290913988.
Savic-Jovcic, V., and B. Stevens (2008), The structure and mesoscale organization of precipitating stratocumulus, *J. Atmos. Sci.*, *65*(5), 1587–1605, doi:10.1175/2007JAS2456.1.
Sharon, T. M., B. A. Albrecht, H. H. Jonsson, P. Minnis, M. M. Khaiyer, T. M. van Reken, J. Seinfeld, and R. Flagan (2006), Aerosol and cloud microphysical characteristics of rifts and gradients in maritime stratocumulus clouds, *J. Atmos. Sci.*, *63*(3), 983–997.
Shinozuka, Y., et al. (2015), The relationship between cloud condensation nuclei (CCN) concentration and light extinction of dried particles: indications of underlying aerosol processes and implications for satellite-based CCN estimates, *Atmos. Chem. Phys. Discuss.*, *15*(2), 2745–2789, doi:10.5194/acpd-15-2745-2015.
Stevens, B., G. Vali, K. Comstock, R. Wood, M. C. Van Zanten, P. H. Austin, C. S. Bretherton, and D. H. Lenschow (2005), Pockets of open cells and drizzle in marine stratocumulus, *Bull. Am. Meteorol. Soc.*, *86*(1), 51–57, doi:10.1175/BAMS-86-1-51.
Terai, C. R., C. S. Bretherton, R. Wood, and G. Painter (2014), Aircraft observations of aerosol, cloud, precipitation, and boundary layer properties in pockets of open cells over the southeast Pacific, *Atmos. Chem. Phys.*, *14*(15), 8071–8088, doi:10.5194/acp-14-8071-2014.
Tomlinson, J. M., R. Li, and D. R. Collins (2007), Physical and chemical properties of the aerosol within the southeastern Pacific marine boundary layer, *J. Geophys. Res.*, *112*, D12211, doi:10.1029/2006JD007771.
Turner, D., S. Clough, J. Liljegren, E. Clothiaux, K. Cady-Pereira, and K. Gaustad (2007), Retrieving liquid water path and precipitable water vapor from the atmospheric radiation measurement (ARM) microwave radiometers, *IEEE Trans. Geosci. Remote Sens.*, *45*(11), 3680–3690, doi:10.1109/TGRS.2007.903703.
Twomey, S., and T. A. Wojciechowski (1969), Observations of the geographical variation of cloud nuclei, *J. Atmos. Sci.*, *26*(4), 648–651, doi:10.1175/1520-0469(1969)26<648:OOTGVO>2.0.CO;2.
VanZanten, M. C., B. Stevens, G. Vali, and D. H. Lenschow (2005), Observations of drizzle in nocturnal marine stratocumulus, *J. Atmos. Sci.*, *62*(1), 88–106.
Wang, H., and G. Feingold (2009), Modeling mesoscale cellular structures and drizzle in marine stratocumulus. Part II: The microphysics and dynamics of the boundary region between open and closed cells, *J. Atmos. Sci.*, *66*(11), 3257–3275, doi:10.1175/2009JAS3120.1.
Wang, H., G. Feingold, R. Wood, and J. Kazil (2010), Modelling microphysical and meteorological controls on precipitation and cloud cellular structures in Southeast Pacific stratocumulus, *Atmos. Chem. Phys.*, *10*(13), 6347–6362, doi:10.5194/acp-10-6347-2010.
Wood, R. (2006), Rate of loss of cloud droplets by coalescence in warm clouds, *J. Geophys. Res.*, *111*, D21205, doi:10.1029/2006JD007553.
Wood, R. (2012), Stratocumulus clouds, *Mon. Weather Rev.*, *140*(8), 2373–2423, doi:10.1175/MWR-D-11-00121.1.
Wood, R., and C. S. Bretherton (2004), Boundary layer depth, entrainment, and decoupling in the cloud-capped subtropical and tropical marine boundary layer, *J. Clim.*, *17*(18), 3576–3588.
Wood, R., C. S. Bretherton, D. Leon, A. D. Clarke, P. Zuidema, G. Allen, and H. Coe (2011), An aircraft case study of the spatial transition from closed to open mesoscale cellular convection over the Southeast Pacific, *Atmos. Chem. Phys.*, *11*(5), 2341–2370, doi:10.5194/acp-11-2341-2011.
Wood, R., D. Leon, M. Lebsock, J. Snider, and A. D. Clarke (2012), Precipitation driving of droplet concentration variability in marine low clouds, *J. Geophys. Res.*, *117*, D19210, doi:10.1029/2012JD018305.
Wood, R., et al. (2015), Clouds, aerosols, and precipitation in the marine boundary layer: An arm mobile facility deployment, *Bull. Amer. Meteor. Soc.*, *96*(3), 419–440, doi:10.1175/BAMS-D-13-00180.1.